JGR Planets

RESEARCH ARTICLE
10.1029/2022JE007427

Temporal Variations in Vertical Cloud Structure of Jupiter's Great Red Spot, Its Surroundings and Oval BA From HST/WFC3 Imaging

Asier Anguiano-Arteaga[1], Santiago Pérez-Hoyos[1], Agustín Sánchez-Lavega[1], José Francisco Sanz-Requena[2], and Patrick G. J. Irwin[3]

[1]Departamento de Física Aplicada, EIB, Universidad del País Vasco UPV/EHU, Bilbao, Spain, [2]Departamento de Física Aplicada, Universidad de Valladolid, Valladolid, Spain, [3]Department of Physics, Atmospheric, Oceanic and Planetary Physics, University of Oxford, Oxford, UK

Key Points:

- A model of the visible reflectivity of the Great Red Spot and its surroundings from 2015 to 2021 shows no significant changes
- Our analysis suggests the presence of two coloring aerosols, the upper one compatible with the chromophore proposed by Carlson et al. (2016, https://doi.org/10.1016/j.icarus.2016.03.008)
- We find that the Oval BA color change between 2016 and 2020 is due to a decrease in the optical thickness of the upper haze

Supporting Information:

Supporting Information may be found in the online version of this article.

Correspondence to:

A. Anguiano-Arteaga,
asier.anguiano@ehu.eus

Citation:

Anguiano-Arteaga, A., Pérez-Hoyos, S., Sánchez-Lavega, A., Sanz-Requena, J. F., & Irwin, P. G. J. (2023). Temporal variations in vertical cloud structure of Jupiter's Great Red Spot, its surroundings and Oval BA from HST/WFC3 imaging. *Journal of Geophysical Research: Planets*, *128*, e2022JE007427. https://doi.org/10.1029/2022JE007427

Received 14 JUN 2022
Accepted 30 AUG 2023

Abstract

In this study, we present the evolution of the properties and vertical distribution of the hazes in Jupiter's Great Red Spot (GRS), its surroundings and Oval BA from 2015 to 2021. To retrieve the main atmospheric parameters, we model the spectral reflectivity of a number of dynamically and/or spectrally interesting regions with a radiative transfer tool that uses an optimal estimator scheme. The spectra of the selected regions are obtained from high-resolution Hubble Space Telescope Wide Field Camera 3 images that cover the spectral range from 200 to 900 nm. The a priori model atmosphere used to describe the various Jovian regions is taken from Anguiano-Arteaga et al. (2021, https://doi.org/10.1029/2021JE006996) for each corresponding area. We find that the biggest variations in the GRS occur in the optical thickness of the stratospheric and tropospheric haze layers starting in 2019 and in the mean size of the tropospheric haze particles in 2018. The absorption spectra of both hazes show little variations among the analyzed regions and years, with the stratospheric haze properties seeming compatible with the chromophore proposed by Carlson et al. (2016, https://doi.org/10.1016/j.icarus.2016.03.008). We report a color change of Oval BA from red to white during these years that, according to our models, can be mostly explained in terms of a decrease in the stratospheric haze optical depth.

Plain Language Summary

The Great Red Spot of Jupiter (GRS) is the largest and longest-lived anticyclone in the solar system atmospheres. Despite having been widely studied, the nature of the aerosol(s) giving the spot its characteristic red color is still unknown, as well as the relation of their creation/destruction mechanisms with dynamics. In 2019, the Great Red Spot started a series of interactions with smaller anticyclones that may have changed its vertical cloud structure, which made the region particularly worthy for our analysis. At the same time, the second largest anticyclone in Jupiter, called Oval BA, changed its color from red to white in 2018, something that also happened in the past (but from white to red) and deserved some attention. We used Hubble Space Telescope images to constrain models of the vertical structure and some relevant atmospheric properties of the hazes in the GRS, its surroundings and Oval BA. We found that most of the changes are related to the thickness of the uppermost coloring layer in the atmosphere, being able to reproduce the observed reflectivity and its temporal and spatial variations. The nature of this layer seems to be compatible with compounds resulting from photochemical reactions in the upper atmosphere.

1. Introduction

The Great Red Spot of Jupiter (GRS) is a prominent feature that has been continuously present in the Jovian atmosphere at least for the last 145 years (Rogers, 1995). During its long lifetime, the GRS has undergone size, shape and color changes. Its size has decreased by half over the past 130 years, with its shape becoming more circular, and it was recently shown to be darkening (Rogers, 1995; Simon et al., 2018; Wong et al., 2021). Changes in the UV and methane band reflectivities have also been measured, implying a change in the vertical distribution of the clouds and hazes (Simon et al., 2018). The aerosol species and physical mechanisms behind the GRS coloration are still unclear and their relation to dynamics remains a challenging question. However, it is commonly accepted that the coloration of the different Jovian areas is explained in terms of the nature and vertical distribution of the hazes, at $P < 1$ bar (Banfield et al., 1998). An interesting chromophore candidate for the GRS was proposed by Carlson et al. (2016): the product from photolyzed ammonia reacting with acetylene. In this

scheme, material in the GRS is raised to the upper troposphere or lower stratosphere and undergoes photochemical reactions that lead to the creation of the coloring agent. Sromovsky et al. (2017) showed that this agent could explain the various degrees of reddish coloration on Jupiter and could act as a universal chromophore (i.e., the same colorant throughout the planet) and, together with Baines et al. (2019), they were able to match GRS spectra using this chromophore in their models. Braude et al. (2020) also concluded that it was possible to model both the GRS and belts of Jupiter with this compound, although a steeper blue absorption was required. This was also found by Pérez-Hoyos et al. (2020) in their North Temperate Belt spectra modeling. Dahl et al. (2021) also found better agreement with their spectra of different Jovian cloud bands by slightly varying the absorption (i.e., imaginary refractive index) of the Carlson et al. (2016) chromophore, but their suggested deviation from that chromophore was opposite to the one found by Braude et al. (2020). Even though radiative transfer analyses were able to fit observations using a single absorbing species, Principal Component Analysis carried out by Simon-Miller et al. (2001) required at least two different coloring agents to explain the color of the GRS and small anticyclones in the northern hemisphere. Following a similar analysis, Ordonez-Etxeberria et al. (2016) also suggested the presence of a second chromophore in a number of Jovian features, but not for the GRS.

As previously mentioned, the relation between Jovian coloration and dynamics is unclear, and events of strong dynamical or coloration changes are an opportunity to gain insight in this respect. We have recently witnessed two phenomena of this kind: the "flakes" episodes in the GRS (Sánchez-Lavega et al., 2021) and the Oval BA color change from red to white. The "flakes" episodes started in 2019, when the GRS suffered the detachment of portions of red material (or "flakes") and distorted its shape after several interactions with a series of relatively small anticyclones coming from the east. Dynamical and radiative transfer analysis performed by Sánchez-Lavega et al. (2021) showed that this was a phenomenon affecting only the upper atmospheric levels ($P < 1$–2 bar).

On the other hand, the Oval BA color change started in 2018 when the ring of reddish clouds surrounding the nucleus turned white. Oval BA formed in the year 2000 after the merger of two white anticyclones present in the South Temperate Belt, one of which was the result of an earlier merger of two white anticyclones (Sánchez-Lavega et al., 1999, 2001). In 2005, the clouds surrounding the oval nucleus started to turn red and this phenomenon was largely studied (Cheng et al., 2008; García-Melendo et al., 2009; Simon-Miller et al., 2006). However, no meaningful dynamical changes were found before or after its reddening (Asay-Davis et al., 2009; Hueso et al., 2009; Marcus et al., 2013; Shetty & Marcus, 2010) nor in its vertical cloud structure (Pérez-Hoyos et al., 2009; Wong et al., 2011). After its reddening, the oval underwent color variations, with some decreases in its redness, but it did not turn completely white until 2019. Unlike the big interest aroused by the 2005–2006 color change, there are no studies on its recent whitening, an inverse color trend when compared to the 2005 change.

We follow in this paper the study of the GRS in 2016 carried out by Anguiano-Arteaga et al. (2021), hereafter referred to as A2021. In that paper, the a priori model atmosphere was obtained by prioritizing the best possible simultaneous spectral and limb-darkening fit of several South Tropical Zone (STrZ) spectra after testing nearly 12,000 models. Two main haze layers were found: a thin layer near the tropopause over a more extended one down to 500 mbar, both showing wavelength-dependent absorption. The stratospheric haze optical depth dominated the overall coloration and, although different chromophore candidates were not directly tested, its retrieved imaginary refractive index spectrum was found to be compatible with the chromophore proposed by Carlson et al. (2016). Specifically, its spectral absorption slope laid within the retrieved error bars, so we focused on this proposed chromophore in particular. This is the most promising candidate to date, which does not possess any additional unobserved spectral feature, as it happens, for example, with the chromophore proposed by Loeffler et al. (2016), as pointed out by Dahl et al. (2021).

In the current work, however, we will be focusing on the temporal evolution of the aerosol properties and vertical cloud distribution of selected regions in the GRS, a variety of surrounding regions and of Oval BA. Addressing this problem is necessary to unveil the nature of the Jovian chromophore(s) and its relation to local dynamics. We also look for an explanation of the observed color changes, the Oval BA whitening being the most striking case. For this purpose, we construct low-spectral resolution spectra from high spatial resolution HST/WFC3 images taken between the years 2015 and 2021, in order to retrieve atmospheric parameters with the NEMESIS radiative transfer suite (Irwin et al., 2008, 2022). The HST/WFC3 data sets are suitable for this aim as they provide images taken in the UV and in two different methane bands (in the best case, as the filter set depends on the observation run), which allow a high sensitivity to the distribution of particles in pressure levels near the tropopause. We will analyze if the model proposed in the previous paper can explain the temporal and spatial variations of the

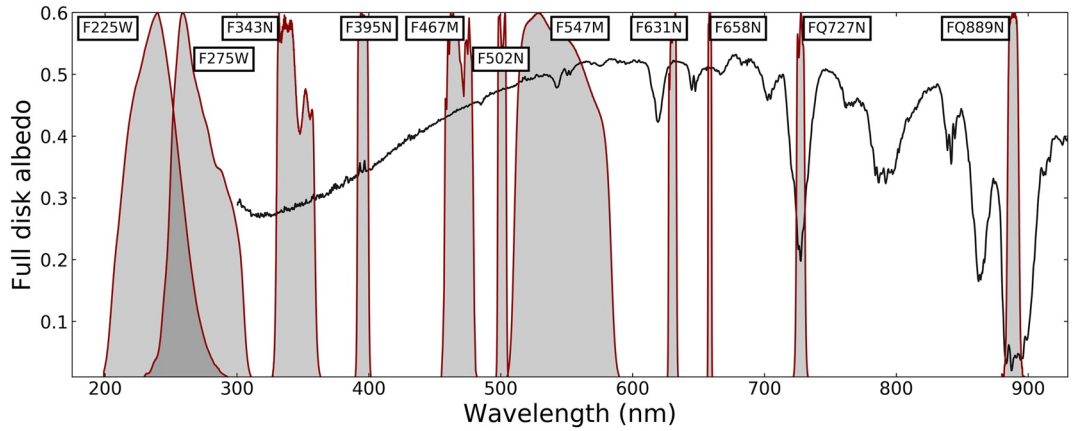

Figure 1. Spectral coverage of Hubble Space Telescope Wide Field Camera 3 filters used in this work overlaid on the full-disk albedo spectrum of Jupiter obtained by Karkoschka (1998). Transmissivity of the filters is scaled to the same maximum.

observed reflectivity, with particular emphasis on the GRS and Oval BA. This will help characterize the vertical haze structure in the GRS area and bring us closer to deciphering the unknowns of its coloration, as well as the changes related to it.

The paper is organized as follows. In Section 2, we briefly describe the HST/WFC3 images, the selected regions that have been studied and different photometric analyses of the GRS area. In Section 3, we present the retrieval procedure and the results for each visit and selected region. In Section 4, we discuss these results and their physical interpretation, also comparing them to prior findings in the literature, and present a sensitivity analysis for our models. Finally, in Section 5, we provide a review of the main conclusions of this work.

2. Observations and Analysis

2.1. HST/WFC3 Observations

For this work, we have used archived images taken by the HST/WFC3 (Dressel, 2021) between years 2015 and 2021. These images cover a wavelength range from the UV to the near-IR with a set of filters sensitive to the cloud structure in the lower stratosphere and upper troposphere –from tens to hundreds mbar- (de Pater et al., 2010a; Pérez-Hoyos et al., 2012a, 2020; Wong et al., 2011), and they have adequate spatial resolution (∼150 km/pixel) for the analysis of relatively small-sized areas. We show in Figure 1 the coverage of HST/WFC3 filters overlaid on the Jovian full-disk albedo spectrum. A summary of the images we used is shown in Table 1. This table also shows the identification label of each observing run discussed hereafter, such as "Wong 2016," "de Pater 2017" or "OPAL 2018," together with the filters and dates corresponding to each of them.

The images were calibrated in absolute reflectivity and projected into cropped latitude-longitude orthogonal map projections of 0.1°/pixel resolution (see Figure 2) after performing a cross-calibration process. This is done in order to reduce the photometric dispersion found among different visits associated with systematic uncertainties in the calibration process. An example of this problem for visit "Wong 2016" is shown in A2021, but it is present throughout the entire time period studied here, with larger discrepancies among images of different campaigns. The images were globally corrected using Equation 1, where m and b were determined for each visit and filter by minimizing central meridian scan differences with respect to visits "de Pater 2018" (for filter F225W), "Wong 2017_02" (for filter FQ727N) and "OPAL 2018" (for the remaining filters). These coefficients are available at the companion repository of this paper (Anguiano-Arteaga et al., 2023).

$$\left(\frac{I}{F}\right)_{\text{corrected}} = \frac{\left(\frac{I}{F}\right)_{\text{uncorrected}} - b}{m} \tag{1}$$

We checked the *I/F* values after the cross-calibration by comparing the corrected full-disk albedos of each visit with the ones given in Karkoschka (1998). We also compared North-to-South *I/F* (see Figure S1 in Supporting Information S1) scans to those of Fry and Sromovsky (2023), finding good agreement of temporal changes, such

Table 1
Summary of Observations Showing the "Grouping Longitudes" (See Section 2.3) of the Great Red Spot Center Relative to the Central Meridian

Visit label and date	Proposal ID and PI	Filters	Lon 1	Lon 2	Lon 3	Lon 4
OPAL 2015 2015/01/19	GO/DD 13937 A. Simon	F275W, F343N, F395N, F502N, F631N, F658N,FQ889N	28°W	28°E	–	–
OPAL 2016 2016/02/09–2016/02/10	GO/DD 14334 A. Simon	F275W, F343N, F395N, F467M, F502N, F631N,F658N, FQ889N	60°W	0°W	60°E	–
Wong 2016 2016/12/11–2016/12/12	GO 14661 M. Wong	F225W, F275W, F343N, F395N, F502N, F631N, FQ727N, FQ889N	60°W	39°W	15°E	–
de Pater 2017 2017/01/11–2017/01/12	GO 14839 I. de Pater	F225W, F275W, F343N, F395N, F502N, F631N, FQ727N, FQ889N	70°W	10°W	50°E	–
Wong 2017_02 2017/02/01–2017/02/02	GO 14661 M. Wong	F225W, F275W, F343N, F395N, F502N, F631N, FQ727N, FQ889N	70°W	44°W	15°E	–
OPAL 2017 2017/04/03	GO/DD 14756 A. Simon	F275W, F343N, F395N, F467M, F502N, F631N,F658N, FQ889N	55°W	30°W	20°E	70°E
Wong 2017_07 2017/07/11	GO 14661 M. Wong	F225W, F343N, F395N, F502N, F631N, FQ727N, FQ889N	35°W	–	–	–
de Pater 2018 2018/02/07	GO 14936 I. de Pater	F275W, F395N, F502N, F631N, FQ727N, FQ889N	45°E	–	–	–
Wong 2018 2018/04/01	GO 14661 M. Wong	F225W, F275W, F343N, F395N, F502N, F631N, FQ727N, FQ889N	50°W	2°W	70°E	–
OPAL 2018 2018/04/17	GO/DD 15262 A. Simon	F275W, F343N, F395N, F467M, F502N, F547M, F631N, F658N,FQ889N	70°W	20°W	40°E	–
Wong 2019 2019/04/09–2019/04/10	GO 14661 GO 15159 M. Wong	F225W, F275W, F343N, F395N, F502N, F631N, FQ727N, FQ889N	50°W	10°E	–	–
OPAL 2019 2019/06/26–2019/06/27	GO/DD 15502 A. Simon	F275W, F343N, F395N, F467M, F502N, F547M, F631N, F658N,FQ889N	25°W	12°E	40°E	–
de Pater 2020 2020/07/22–2020/07/23	GO 16053 I. de Pater	F225W, F275W, F395N, F502N, F631N, FQ727N, FQ889N	60°W	2°W	–	–
OPAL 2020_08 2020/08/25	GO/DD 15929 A. Simon	F275W, F395N, F467M, F502N, F631N, F658N,FQ889N	35°W	15°E	–	–
OPAL 2020_09 2020/09/20	GO/DD 15929 A. Simon	F275W, F343N, F395N, F467M, F502N, F631N, F658N, FQ889N	40°W	–	–	–
OPAL 2021 2021/09/04	GO/DD 16266 A. Simon	F275W, F343N, F395N, F467M, F502N, F631N, F658N, FQ889N	50°W	6°E	–	–

Note. Note that each region, other than the GRS nucleus, has a latitude/longitude displacement with respect to that point that can change from one observing run to the following.

as the blue brightness drop in the Equatorial Zone (EZ). In both cases, the cross-calibration process was shown to properly address the dispersion problem. Specifically, the average dispersion in the full-disk albedos before the correction was ∼12%, with a remarkable 35%–40% dispersion in the UV. After correcting, the dispersion was reduced to less than 2%. This procedure is fully explained in the supplementary information of A2021.

Quad filter images are affected by fringing. According to Wong (2010), the measured amplitude of fringing in WFC3 images is ∼5% for filter FQ889N and 1% for FQ727N. This problem is accounted for by assuming a 10% measurement uncertainty, which is the typical value in HST/WFC3 absolute calibration (Dressel, 2021), similar to Toledo et al. (2019).

2.2. Region Selection

For this study, we have selected a number of regions that are interesting from a dynamical and/or a spectral point of view, in order to get a full description of the considered area and its temporal evolution. We have also analyzed Oval BA, as it underwent a noteworthy color change from red to white during the time span covered by this

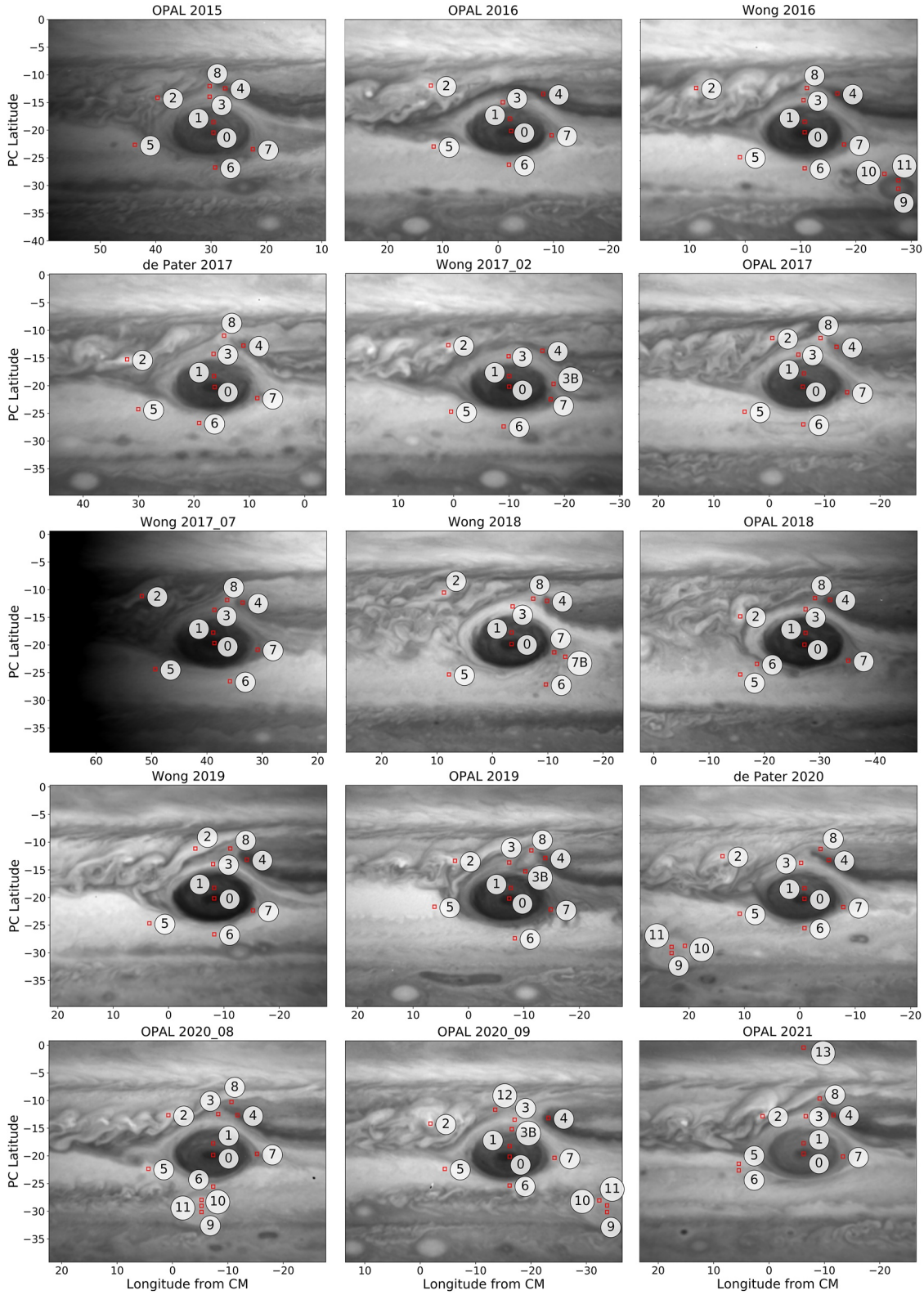

Figure 2. Cropped maps (0.1°/pixel resolution) in the F502N filter (blue) showing the Great Red Spot of Jupiter for different HST visits (Table 1). The gray scale *I/F* range goes from 0.3 (black) to 0.9 (white) in all panels. The "Wong 2017_07" map is scaled (by a factor ≈1.17), as proximity to the limb made it too dark. Visit "de Pater 2018" is not included for graphic purposes. The 0.5° × 0.5° regions selected for further radiative transfer analysis are marked in each map. Oval BA appears approximately at 30°S in years 2016 and 2020. Please note that degrees (°) refer here to latitude/longitude and not to angular size on the sky.

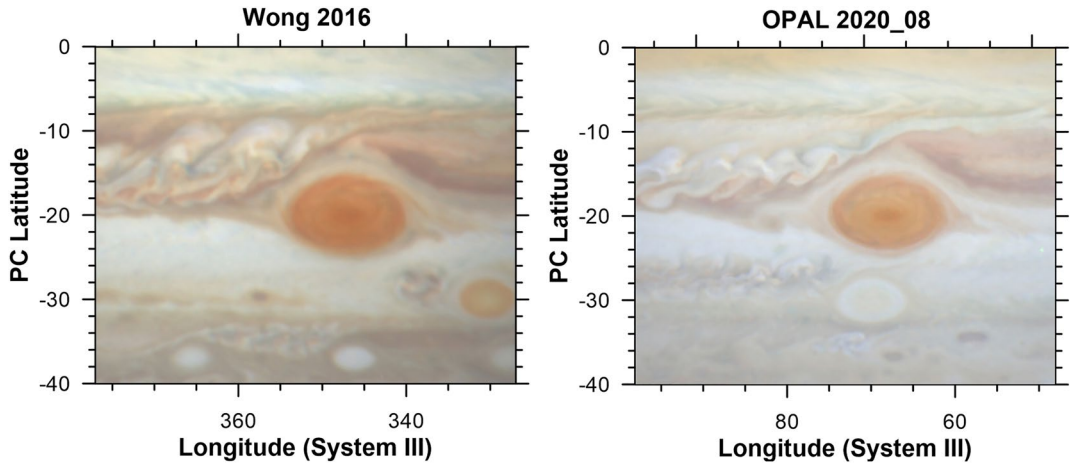

Figure 3. Maps showing the color change undergone by Oval BA between years 2016 (lat = −30°, lon = 330°, CM = 356.2°) and 2020 (lat = −30°, lon = 70°, CM = 74.4°). The RGB images are constructed from Hubble Space Telescope Wide Field Camera 3 images used in this work with R = F631N, G = F502N, and B = F395N.

work. This color change resembled the 2005–2006 reddening (Cheng et al., 2008; García-Melendo et al., 2009; Simon-Miller et al., 2006) but in the opposite direction.

The regions analyzed in each HST visit are shown in Figure 2. For each visit, we tried to select regions analogous to the ones shown by A2021and, therefore, the range of coverage of the cropped maps and the position of the GRS within that coverage is the same as that of that paper. However, the location relative to the GRS of the selected regions is slightly different from visit to visit because of the morphological changes in the GRS area and the dynamical nature of many of the features.

Regions 0 and 1 are the dark nucleus and interior of the GRS, respectively. They have the strongest blue wavelength absorption (see Figure 2). Region 2 is located northwest of the GRS, in areas where vigorous upwelling motions of bright clouds are expected due to moist convection (Hueso et al., 2002). Region 3 is located in the area commonly known as the hollow (Rogers, 1995; Sánchez-Lavega et al., 2018). In the case of "Wong 2017_02," "OPAL 2019," and "OPAL 2020_09," another region (3B) was also selected in the hollow in order to account for an area showing different spectral characteristics. Region 4 is placed in the dark clouds that are carried to the circulation of the GRS by the westward jet ($u \approx -60$ m s^{-1}) located at 20° S (Rogers, 1995).

Regions 5 and 6 are both located in the STrZ, but they show slightly different spectral behavior (see Section 2.5). Region 7 is selected in the area of dark clouds southeast of the GRS, known as "lacrimal gland" (A2021), and, along with the GRS eastern flank, it was the exit for the reddish material (the so called "flakes") pulled off the GRS after its interaction with smaller anticyclones (Sánchez-Lavega et al., 2021). In "Wong 2018" another region (7B) was selected, since the "lacrimal gland" showed a remarkable spectral dichotomy (see Section 2.5). Region 8 is located in the "chimney" (Rogers, 2019), a discontinuity in the flow of low-albedo clouds at the northern extent of the GRS area. The discontinuity is not always present, as can be seen in visits "OPAL 2016" and "Wong 2017_02," and when this happens, region 8 is not selected.

We have also included three regions (9, 10, and 11) located in Oval BA, but only in the visits in which the oval was present in the cropped maps ("Wong 2016," "de Pater 2020," "OPAL 2020_08," and "OPAL 2020_09"), in order to analyze the color change of the oval between years 2016 and 2020 (see Figure 3). Region 9 is the nucleus of Oval BA, region 10 is the periphery of white clouds (which is also part of the circulation of the oval) and region 11 is an interior ring in which the color change was most significant. Region 12 is only present in "OPAL 2020_09," and it was chosen because of its particular spectral classification (see Section 2.5). Finally, Region 13 is located in the EZ and is only selected in visit "OPAL 2021", since it showed a noticeable reddish coloration at that time.

2.3. Spectra Construction

For every visit, we constructed spectra for each selected region and for different viewing geometries by following the same procedure as in A2021. We do so because the NEMESIS version we used demands spectra with two or

more wavelengths for each viewing geometry. The main advantage of simultaneously fitting spectra corresponding to different viewing geometries is that it helps to break inherent degeneracies in the radiative transfer calculations in the optical wavelength regime. To construct the spectra, we first identified the "grouping longitudes" relative to the Central Meridian (CM) around which the GRS is present in as many images and filters as possible. We then built the spectra by performing a weighted average of the *I*/*F* values of the same filter images with the GRS center located in ±10° from the grouping longitudes. The weights were given by a Gaussian curve centered at the grouping longitudes and with FWHM = 5° and unity peak value. Points located further than ±80° from the CM were not considered to avoid navigation issues. The uncertainty introduced by the navigation of the images and the spectra construction is non-negligible and difficult to constrain, and thus we set a minimum error of 10% following A2021. This strategy may give more weight to narrow-band filters, which are the most uncertain, with errors typically ranging about 5%–10% (Calamida et al., 2021). The grouping longitudes (Lon 1 to Lon 4) of all the visits are shown in Table 1.

2.4. Color Analysis

We use two photometric indices introduced by Sánchez-Lavega et al. (2013) to analyze the selected Jovian areas in terms of color and altitude and/or opacity. These indices are the Color Index (CI) and the Altitude/Opacity Index (AOI), and they are defined as the reflectivity ratio of the F395N to F631N and FQ889N to F275W, respectively. Low CI values correspond to reddish areas, while high values are obtained for white or blue regions. Similarly, AOI values are correlated with cloud top altitude, since high atmospheric features are bright in the methane absorption bands and dark in the UV, as a consequence of particulate absorption. Please note that cloud top altitude depends on the vertical distribution of the haze opacity and hence AOI is not just simply an altimetry value.

Figure 4 shows the temporal evolution of the AOI and CI values for the selected regions (except 12 and 13 as they are present in a single visit). To make these plots, we performed a Lambertian correction in filters F395N, F631N, and FQ889N to reduce the effects induced by changes in the viewing geometry among the maps corresponding to these filters (Ordonez-Etxeberria et al., 2016). For the F275W filter, we performed a Minnaert correction (Sánchez-Lavega, 2011), as it was more suitable due to the strong Rayleigh scattering close to the limb, by following the same procedure as in A2021. The limb-darkening exponents are calculated from each filter image. Statistical information on Figure 4 data can be found in Table 2. There are several contributions to the AOI and CI errors. Together with the uncertainty of the HST photometric calibration, geometric corrections also induce some error in these magnitudes. Since the effect of the corrections is difficult to constrain, we adopt an error of 10%, which is the typical value in HST/WFC3 absolute calibration (Dressel, 2021).

From Figure 4 it is clear that regions 0 and 1 (the GRS nucleus and interior) are distinct in terms of AOI and also of CI, although in the latter we find a greater dispersion in the regions outside the GRS. The AOI indices for regions 0 and 1 indicate a decrease in altitude/opacity from 2016 to 2021. On the other hand, the CI values for those regions increase, indicating that the GRS became less reddish in recent years, as also shown in Figure S3 in Supporting Information S1. The AOI values for regions 9 and 11 (Oval BA nucleus and ring) also show a slight decrease from 2016 to 2020, whilst region 10 (the periphery of the oval) shows no major temporal differences. This is also apparent from Figure S2 in Supporting Information S1. The CI values of these regions, however, show an overall increase from 2016 to 2021, with the most noticeable change in regions 9 and 11. This is in agreement with the brightness variations observed in Oval BA in Figure 2 maps. However, the high variability in some other regions, such as regions 2 (convective storms area), 3 (hollow), 7 (lacrimal gland), and 8 (chimney), is due to the fact that they are highly dynamical and may change abruptly from visit to visit, as can be seen in Figure 2. A word of caution must be raised regarding the AOI/CI values in visit "Wong 2017_07" as they are severely affected by limb-darkening effects.

2.5. Spectral Clustering

We use here the *k*-means clustering method (Jancey, 1966; Pérez-Hoyos et al., 2012b) to classify each point in the maps according to its spectral characteristics, as done by A2021. The *k*-means algorithm groups each pixel of the cropped maps in the specified number of clusters by minimizing the squared Euclidean distance of each pixel spectrum to the nearest cluster centroid (i.e., the pixel/spectra that best represents that cluster). We proceeded as follows: for all the considered visits, we selected a map with the GRS as close to the CM as possible for each

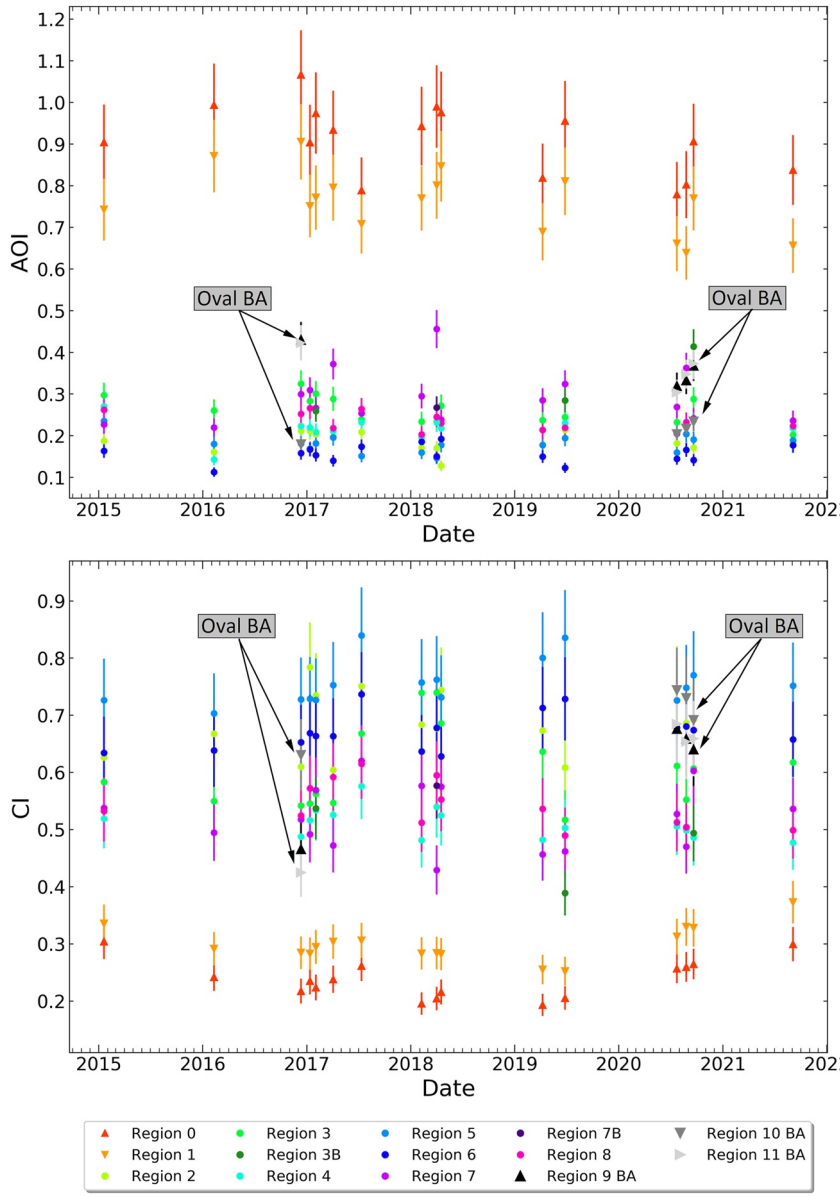

Figure 4. Altitude/Opacity Index (upper panel) and Color Index (lower panel) versus time.

available filter. We then corrected the maps following a Minnaert law (Sánchez-Lavega, 2011), and after the correction, the spectra at each pixel were classified in six clusters using a *k*-means algorithm (Sculley, 2010). We set the number of clusters to six because for a larger number, we obtained new classifications that were due to limb-darkening and not intrinsic spectral differences. The resulting clustering for each visit is shown in Figures 5 and 6.

From Figures 5 and 6, it is apparent how spectrally different the GRS is from other surrounding areas, except in visit "OPAL 2021," in which the EZ also looks reddish and bright/faint in the methane band/UV filter and is therefore classified together with the GRS. It is also clear from Figures 5 and 6 that the STrZ is mainly split in two different clusters, supporting the separated analysis of regions 5 and 6, as discussed above. Region 7B was also selected because the "lacrimal gland" in visit "Wong 2018" is split in two different clusters. In general, for each visit, our region selection encompasses all the found clusters. Region 12 in visit "OPAL 2020_09" was selected because of this, since it belongs to an unsampled cluster. The change in the Oval BA clustering from 2016 to 2020 is also noteworthy, as it reveals its color change from reddish to whitish.

Table 2
Mean, Maximum, and Minimum AOI (Altitude/Opacity Index = I/F(FQ889N)/I/F(F275W)) and CI (Color Index = I/F(F395)/I/F(F631)) Values of the Studied Regions

Region	<AOI> ± σ	AOI_{max}	AOI_{min}	<CI> ± σ	CI_{max}	CI_{min}
0	0.91 ± 0.08	1.07	0.78	0.24 ± 0.03	0.3	0.19
1	0.76 ± 0.08	0.91	0.64	0.3 ± 0.03	0.37	0.25
2	0.19 ± 0.02	0.21	0.13	0.68 ± 0.06	0.78	0.54
3	0.26 ± 0.03	0.33	0.2	0.61 ± 0.07	0.74	0.52
3B	0.32 ± 0.07	0.41	0.26	0.47 ± 0.06	0.54	0.39
4	0.22 ± 0.03	0.27	0.14	0.51 ± 0.03	0.58	0.48
5	0.18 ± 0.02	0.23	0.15	0.76 ± 0.04	0.84	0.7
6	0.16 ± 0.02	0.19	0.11	0.67 ± 0.03	0.74	0.63
7	0.29 ± 0.06	0.46	0.22	0.52 ± 0.05	0.62	0.43
7B	0.27 ± 0.0	0.27	0.27	0.58 ± 0.0	0.58	0.58
8	0.23 ± 0.02	0.27	0.2	0.54 ± 0.04	0.61	0.49
9 (BA)	0.36 ± 0.04	0.43	0.32	0.61 ± 0.08	0.68	0.47
10 (BA)	0.21 ± 0.02	0.23	0.18	0.7 ± 0.04	0.74	0.63
11 (BA)	0.36 ± 0.04	0.42	0.3	0.6 ± 0.1	0.69	0.42

An interesting application of the spectral clustering is that it allows the extrapolation of the retrieved properties of the selected regions to other areas of the map with similar spectra belonging to the same cluster, as done by A2021 and as will be shown in Section 4. However, it must be noted that our results correspond only to the selected regions, and they should be regarded only as a first approximation (e.g., as a priori models) to other areas falling within the same spectral cluster.

3. Radiative Transfer Modeling

We performed the retrieval of atmospheric parameters from the measured spectra with the NEMESIS radiative transfer package (Irwin et al., 2008, 2022). A brief description of NEMESIS is given in A2021. The vertical temperature profile and the atmospheric gaseous composition (assumed to be a mixture of H_2, He and CH_4) are taken from Taylor et al. (2004). Particle scattering is modeled using a double Henyey-Greenstein smoothed approximation of Mie phase functions to get rid of backscatter fine structure. We do not consider the polarization of scattered light as it is relatively weak in the latitudes our analyzed regions fall into (McLean et al., 2017). We also do not include ammonia in our atmospheric model since it is depleted in upper atmospheric levels (Taylor et al., 2004) and the only filter potentially sensitive to it is F547M. This filter encompasses the band centered at 552 nm (Irwin et al., 2019), but it is a relatively weak band and falls in a wide filter that is only present in few visits. When we tested the convolution of the F547M filter with the Jovian full-disk albedo (Karkoschka, 1998) with and without the ammonia absorption band, we found differences lower than 1%. Therefore, this absorption band is negligible for our purposes. Rayleigh scattering is accounted for in the calculations. We do not consider Raman scattering, as its effect in the modeling is well within the assumed uncertainty, although it is an important effect at shorter wavelengths (Fry & Sromovsky, 2023).

3.1. A Priori Model Atmospheres

The a priori model atmosphere presented in A2021 was the outcome of the analysis of numerous retrievals from STrZ spectra. The main point was to prioritize the best simultaneous spectral and limb-darkening adjustments of a relatively calm and standard region that can be taken as a reference (Sánchez-Lavega et al., 2013). This region also has the advantage of being zonally homogeneous, thus providing a good sampling of its limb-darkening. The resulting a priori model was applied to all the selected regions in the cited work. In order to be able to fit regions with spectra significantly different from that of the STrZ, we set large initial parameter uncertainties, so we were able to retrieve parameter values very different from the initial ones.

In this work, we followed a different approach: for each selected region, we use as a priori parameter values the ones retrieved for the analogous region in visit "Wong 2016," which is the visit studied in A2021. In other words, the models presented here use the outputs from retrievals that used spectra from "Wong 2016." This was done for two main reasons. First, this procedure allowed reducing the retrieved errors to more constrained values, since they depend on the input errors and these were now smaller. Second, this approach helped to avoid another family of solutions that also provided marginally acceptable fits but was not supported in cases with stronger limb-darkening constraints and lacked self-consistency when comparing the whole time period in this work.

Table 3 shows the set of parameters used to define the hazes and their type (free or fixed). The vertical distribution of stratospheric and tropospheric hazes is parameterized with three model parameters: the bottom pressure (P_{bot}), the maximum haze abundance reached at bottom pressure (N_{peak}) and the ratio of the aerosol to the gas scale height (fsh). In Table 3, however, we include the optical depth at 900 nm (τ) instead of N_{peak} because it is a more straightforward and intuitive magnitude to interpret. In our model, there is no top pressure defined as such, and the haze abundance decreases exponentially with increasing altitude as ruled by the fractional scale height. We will later introduce the pressure level at which optical depth equals unity as a proxy to a cloud top level, but this is never used as a free parameter in the modeling. The imaginary part of the refractive index m_i is a free

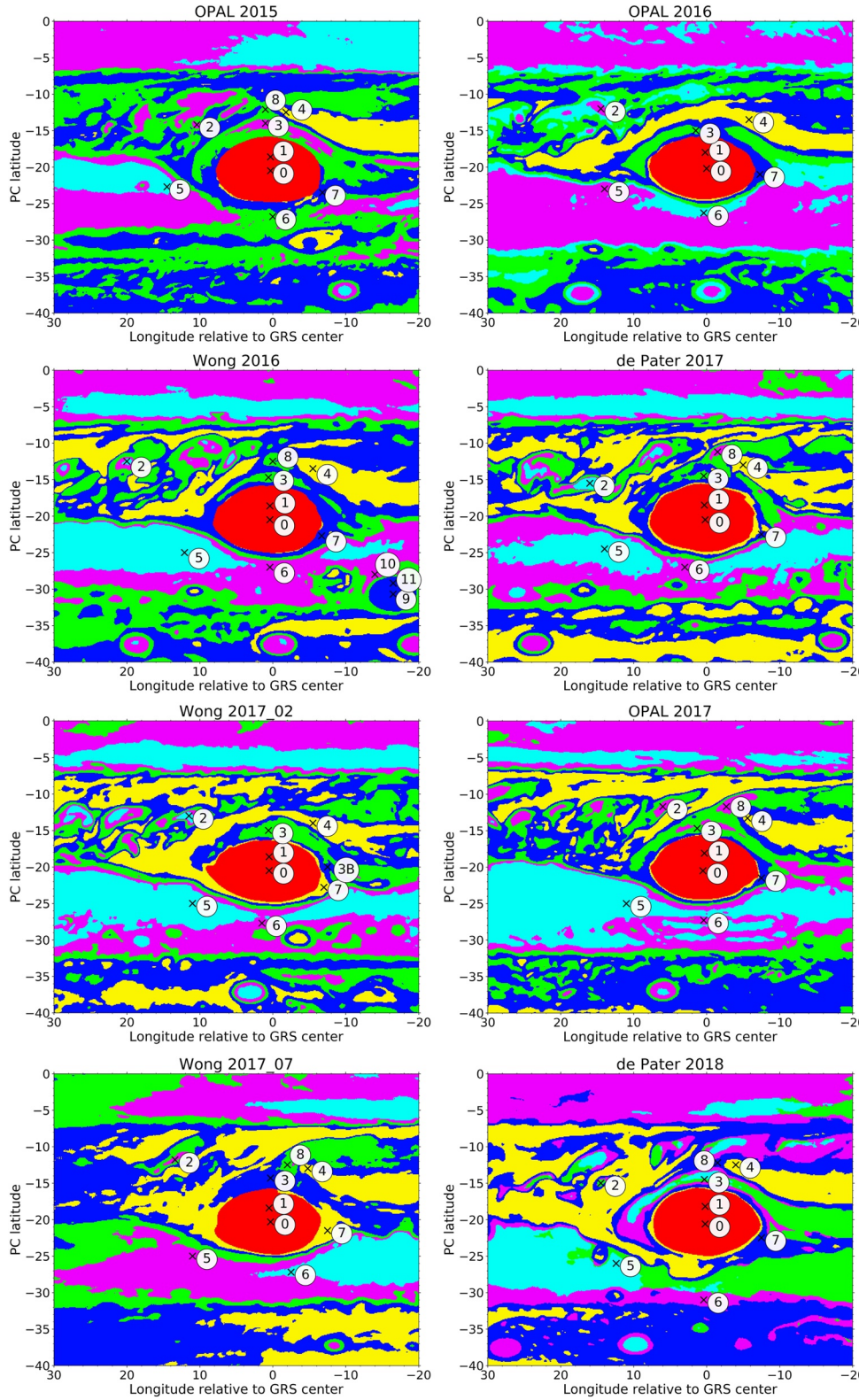

Figure 5. Spectral clustering of the Great Red Spot of Jupiter surroundings from 2015 to 2018. Each color corresponds to one of the clusters found with the *k*-means algorithm (Sculley, 2010). The black crosses show the selected regions. Map in visit "Wong 2017_07" is severely affected by limb-darkening effects.

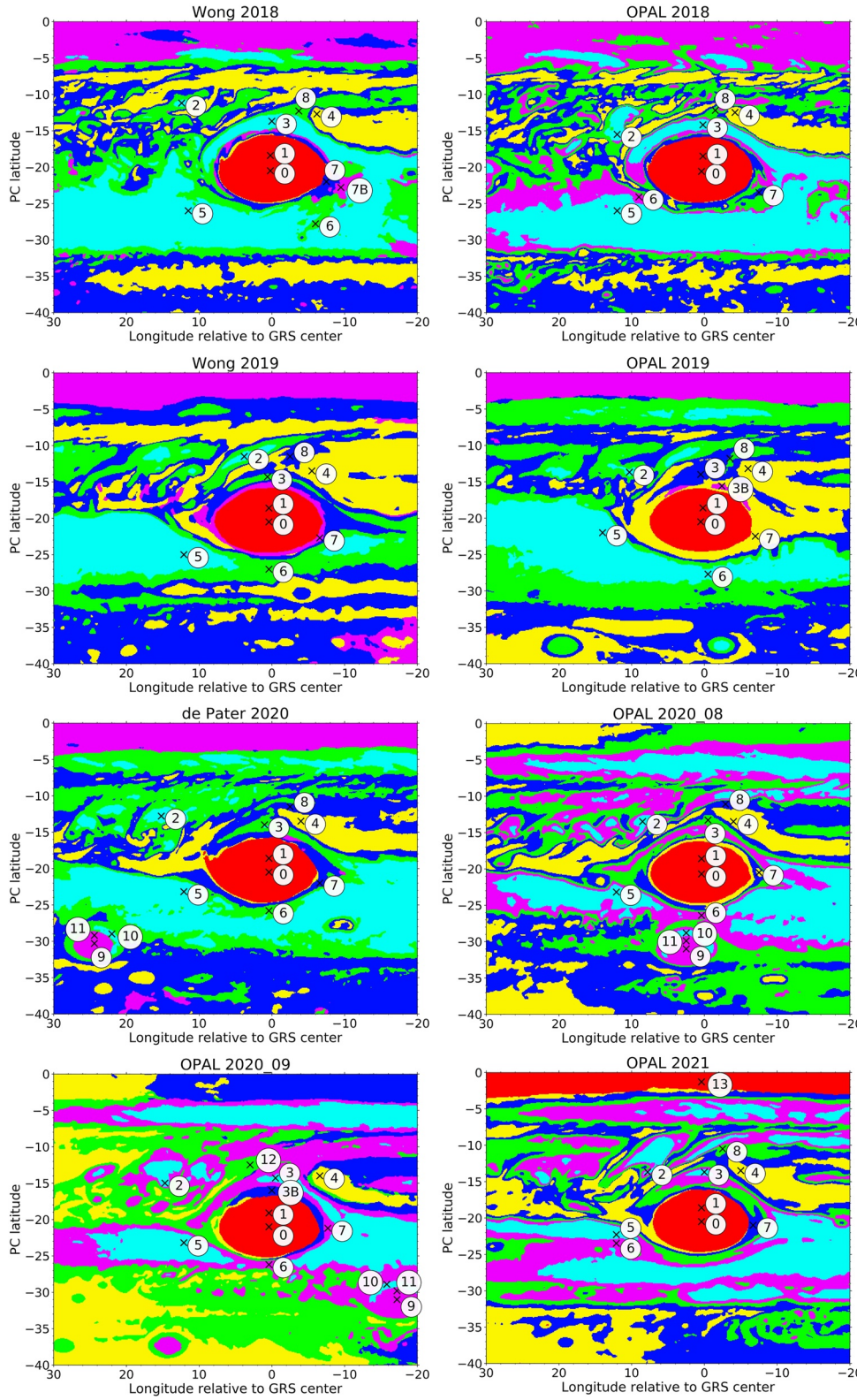

Figure 6. Spectral clustering of the Great Red Spot of Jupiter surroundings from 2018 to 2021. Each color corresponds to one of the clusters found with the *k*-means algorithm (Sculley, 2010). The black crosses show the selected regions. Map in visit "OPAL 2020_09" is severely affected by limb-darkening effects.

Table 3
Fixed and Free Parameters Used in the Modeling and Their Corresponding a priori Values

Layer	Parameter	Type	A priori values (region 0/GRS nucleus)
Stratospheric haze	P_{bot} [a]	Free	110^{+90}_{-50} mbar
	τ_{str}(900 nm)	Free	1.8 ± 0.6
	fsh	Free	0.08 ± 0.09
	m_i	Free/Fixed	See Wong 2016 in Figure 9
	m_r[a](900 nm)	Fixed	1.65
	r_{eff}	Free	0.29 ± 0.07 μm
	σ_{eff}	Fixed	0.1
Tropospheric haze	P_{bot}	Free	500^{+300}_{-200} mbar
	τ_{trop}(900 nm)	Free	30 ± 20
	fsh	Free	0.34 ± 0.07
	m_i	Free/Fixed	See Wong 2016 in Figure 9
	m_r[b](900 nm)	Fixed	1.43
	r_{eff}	Free	2 ± 1 μm
	σ_{eff}	Fixed	0.1

Note. Fixed parameters are set as in A2021.
[a]Zhang et al. (2013). [b]Pérez-Hoyos et al. (2020).

parameter for $\lambda \leq 631$ nm in the stratospheric case and for $\lambda \leq 467$ nm in the tropospheric case, while it is fixed for longer wavelengths, following the results of A2021. The particle mean effective radius r_{eff} is also a free parameter, and the width of the assumed log-normal particle size distribution is σ_{eff}. For an illustrative representation of the atmosphere parameterization, see Figure 11.

We only include in Table 3 the a priori values applied to the region 0/GRS nucleus for clarity. However, a priori values of any region can be found in the corresponding region values for "Wong 2016" in Table S1 in Supporting Information S1. On the other hand, the a priori imaginary refractive indices of the Oval BA regions and of the remaining ones are shown in the "Wong 2016" panels of Figures 9 and 10, respectively.

As stated in A2021, the employed models are insensitive to the bottom cloud presumably formed by NH_3, and are therefore not included on Table 3. In other words, our retrievals remain the same after varying the parameters defining this cloud deck, so no information about it can be gained with our model. This issue will be addressed in more detail in the sensitivity analysis in Section 4.4. It should also be noted that generally there is no overlapping of the stratospheric and tropospheric haze.

3.2. Retrieval of Selected Regions

A summary of the retrieved parameters, excluding imaginary refractive indices, is shown in Table S1 in Supporting Information S1. Some example spectra and the corresponding fits can be found in Figure 7. For all the analyzed regions and visits, the stratospheric and tropospheric haze bottom pressures vary very little. More specifically, we find mean values and standard deviations of 110 ± 10 and 495 ± 1 mbar for the stratospheric and tropospheric hazes, respectively. In general terms, we found reasonable fits attending to the error function χ^2/N (i.e., fits with χ^2/N values close to or less than 1). Worthy of note is "OPAL 2017," as it is the only visit with spectra corresponding to four different viewing geometries. Despite being the most restrictive data set in terms of limb-darkening constraints (which is useful to break degeneracies in our wavelength regime), we found good fits in all the selected regions. In addition, no overfitting of the data was found, since we only get very low χ^2/N values in cases with a lack of observational constraints (fewer filters or geometries available). In general, we have 14–18 free parameters (Table 3), depending on the number of filters available for each visit, which limits the number of imaginary refractive indices to be fitted. We do not include the bottom cloud optical depth as we are insensitive to it. The number of free parameters is further reduced by two if we exclude the bottom pressures of the stratospheric and tropospheric hazes, which actually vary very little. When comparing the number of free

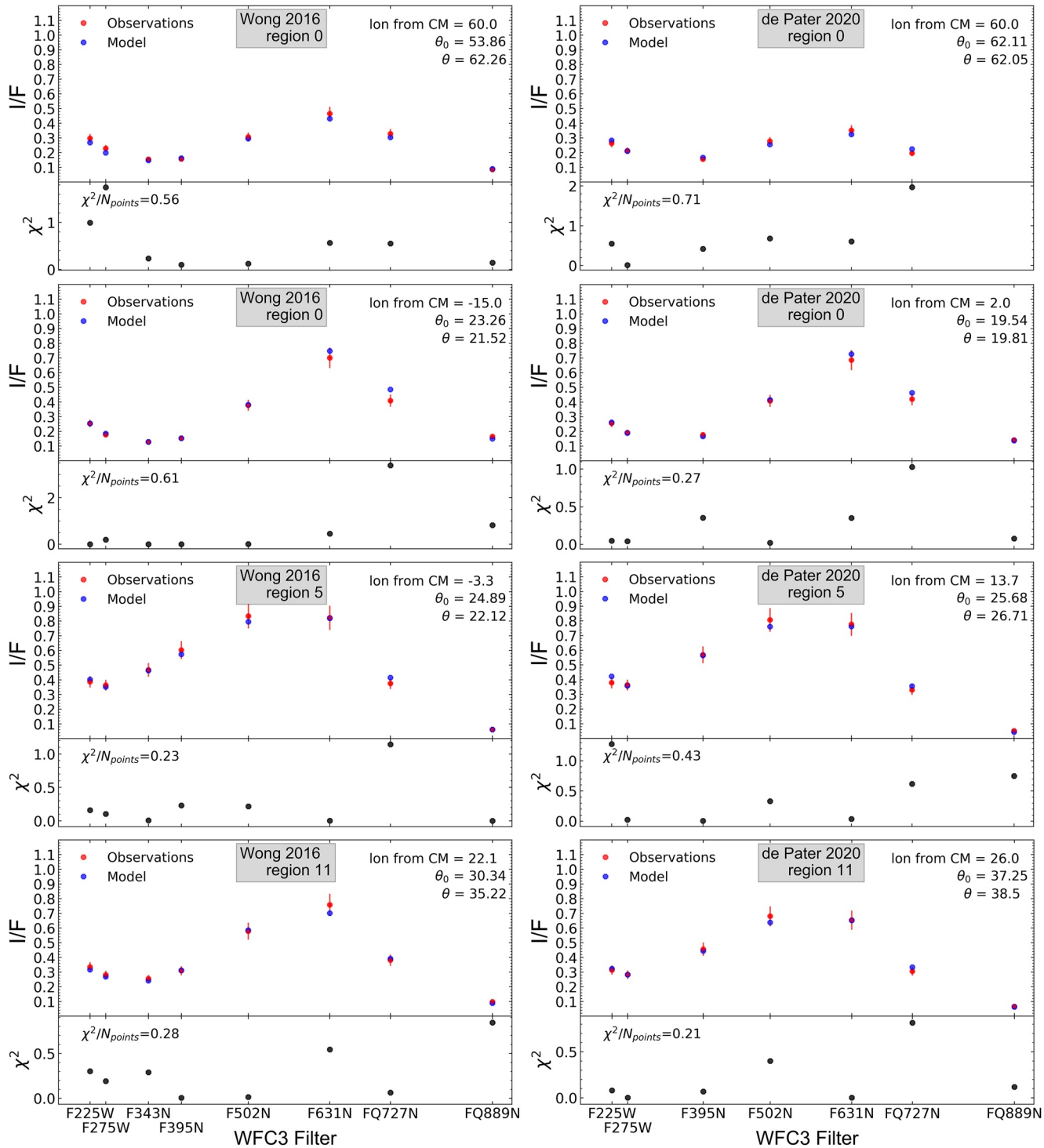

Figure 7. Example spectra and fits for regions 0 (Great Red Spot of Jupiter [GRS] nucleus), 5 (South Tropical Zone), and 11 (Oval BA ring) for visits "Wong 2016" and "de Pater 2020." For region 0, we show the spectra in two different viewing geometries in order to show the limb-darkening behavior of the GRS. The different viewing geometries were fit simultaneously (together with an additional viewing geometry in the case of "Wong 2016"). θ_0 and θ are the incidence and emission zenith angles of radiation, respectively. Please note that the spectral slope between filters F502N and F631N is flattened in 2020, indicating the color change undergone by Oval BA.

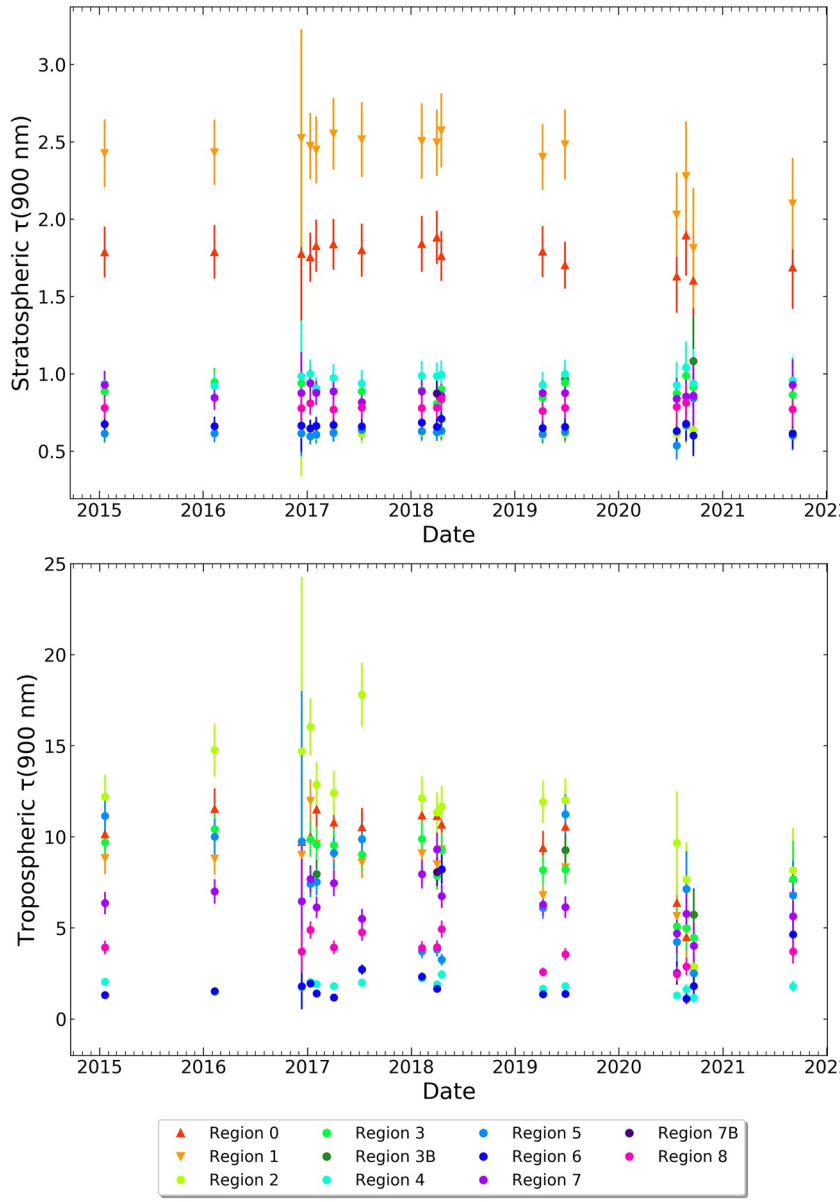

Figure 8. Retrieved stratospheric and tropospheric optical depths at 900 nm for regions from 0 to 8 (regions in the Great Red Spot of Jupiter and its surroundings). Tropospheric values were computed down to the 330 mbar level to allow a better comparison among different regions. Total optical thickness values can be found in Table S1 in Supporting Information S1.

parameters to that of observational points (or constraints, Table 1), which span from 6 to 31, we find that 13 visits out of the total 16 are reasonably constrained, that is, they have more or equal constraints than free parameters. The less constrained visits are "Wong 2017_07," "de Pater 2018," and "OPAL 2020_09," so results for these are less reliable. However, tests fixing more parameters revealed no significant differences and the results in these visits are consistent with the better constrained cases, such as "OPAL 2017," and are thus included.

Figure 8 shows the evolution of the optical depths at 900 nm for regions from 0 to 8 (regions 12 and 13 are only present in a single visit and Oval BA regions are analyzed separately). "Wong 2016" has larger error bars because all the regions were fitted with the same a priori model (A2021), as explained in the previous section. The implications of the data shown in Figure 8 on color evolution are discussed in Section 4.

The evolution of the stratospheric and tropospheric optical depths for Oval BA regions is shown in Table 4. There is a general decrease from 2016 to 2020, except for the stratospheric haze in region 10 (Oval BA periphery). The implications of these results on color evolution are also discussed in Section 4.

Table 4
Optical Depths at 900 nm for Oval BA Regions

	Region 9 Oval BA nucleus		Region 10 Oval BA periphery		Region 11 Oval BA ring	
	τ_{str}	τ_{trop}	τ_{str}	τ_{trop}	τ_{str}	τ_{trop}
2016	0.8 ± 0.3	4 ± 3	0.7 ± 0.2	2 ± 1	1.2 ± 0.5	3 ± 2
2020	0.70 ± 0.07	2.3 ± 0.5	0.63 ± 0.02	2.4 ± 0.3	0.79 ± 0.09	3 ± 1

Note. Please note that the tropospheric optical depths are cut off at 330 mbar. The 2020 values are averages that have been weighted with the inverse of the optical depth variance (weight = $(\Delta\tau)^{-2}$).

4. Interpretation of the Results

4.1. Oval BA

The Oval BA underwent a color change from red to white between years 2018 and 2019. Our results suggest that the main change in region 11 (Oval BA ring) from 2016 (red) to 2020 (white) was a decrease in optical depth of

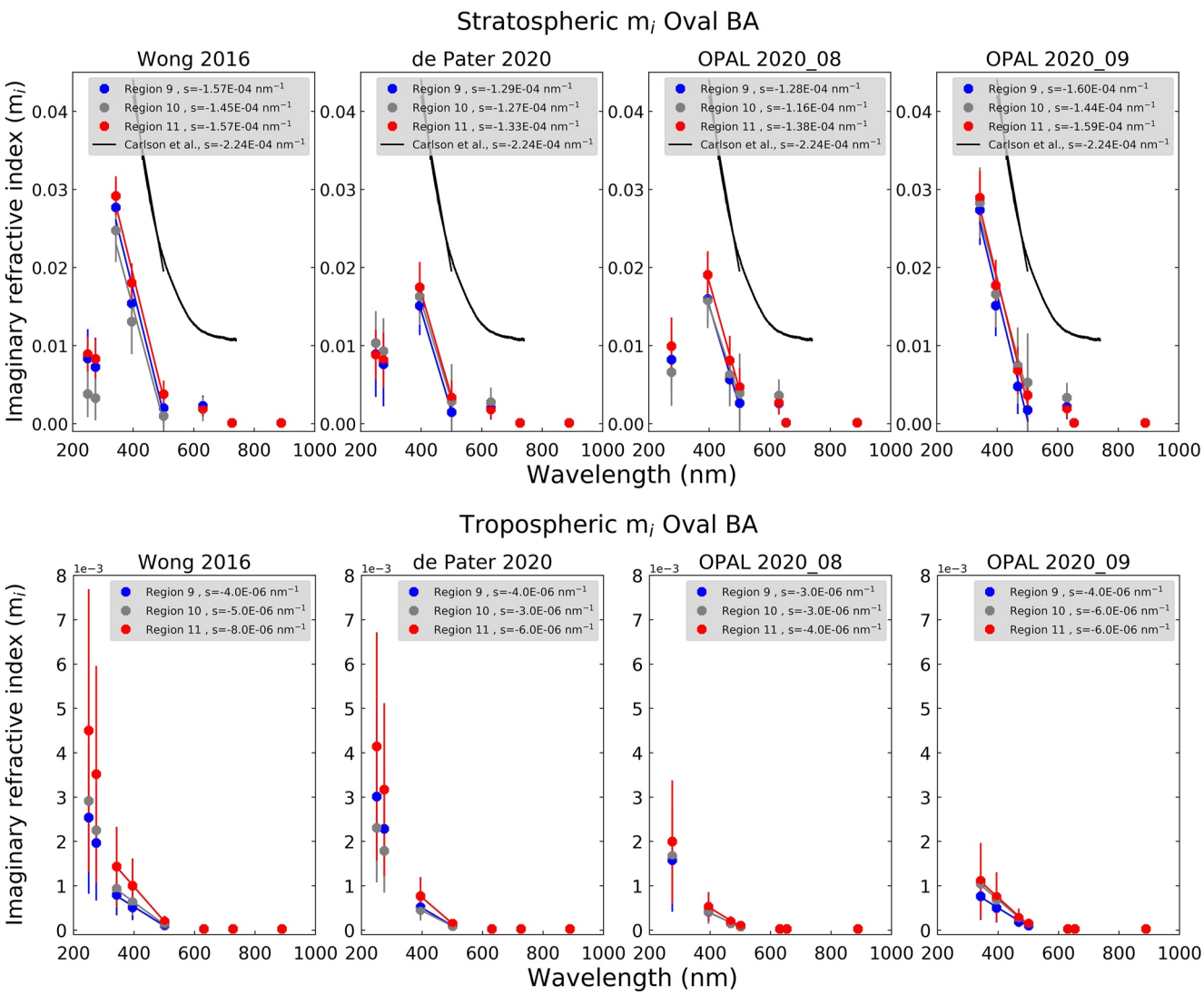

Figure 9. Evolution of stratospheric and tropospheric imaginary refractive indices for the analyzed Oval BA regions 9–11. The retrieved spectral slopes *s* in the 350–500 nm range are given in each plot, together with Carlson et al. (2016)'s laboratory chromophore (black lines, only in the stratospheric case).

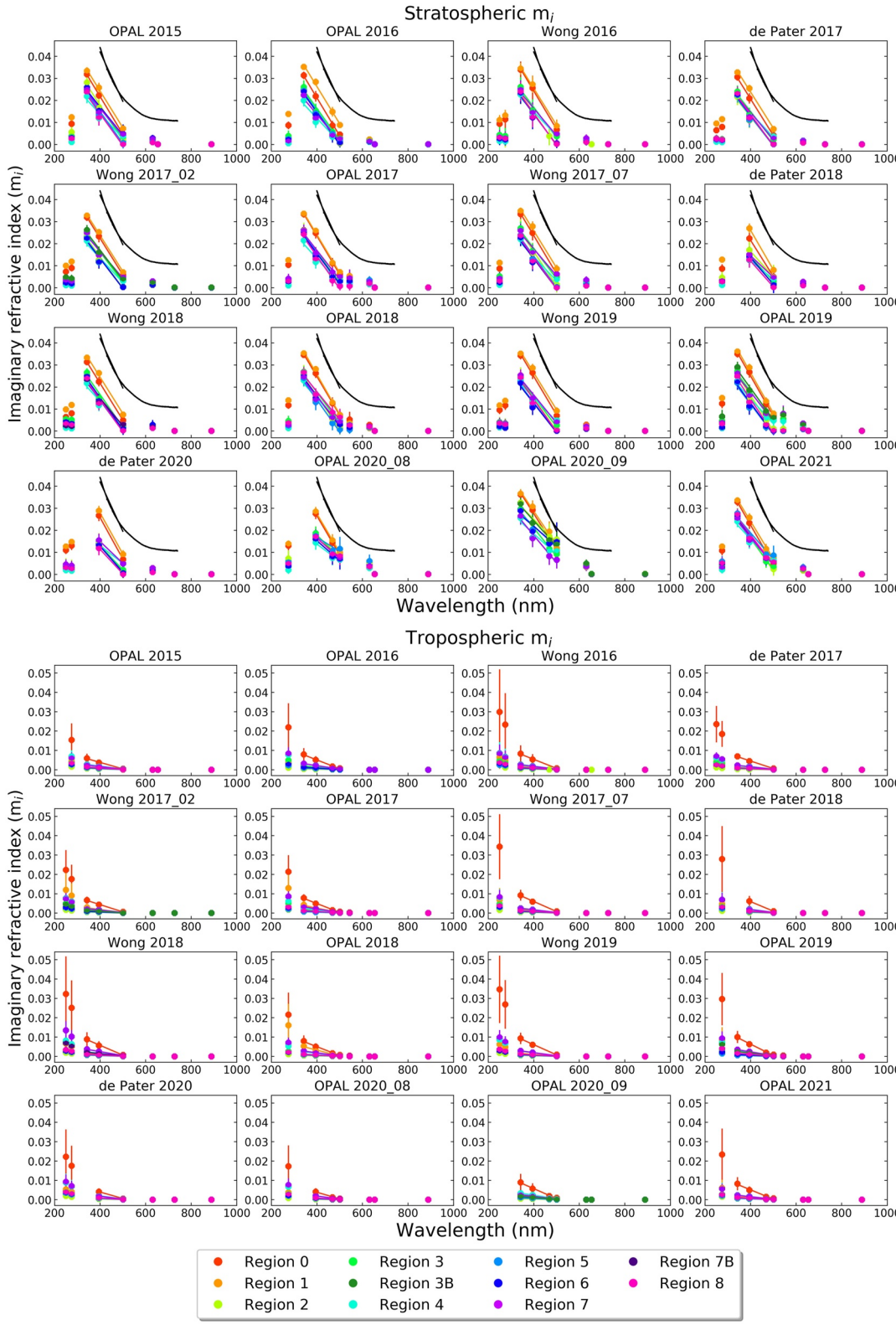

Figure 10. Evolution of the stratospheric and tropospheric imaginary refractive indices for the Great Red Spot of Jupiter and adjacent regions from 0 to 8. The black lines in the stratospheric case are Carlson et al. (2016)'s laboratory chromophore values.

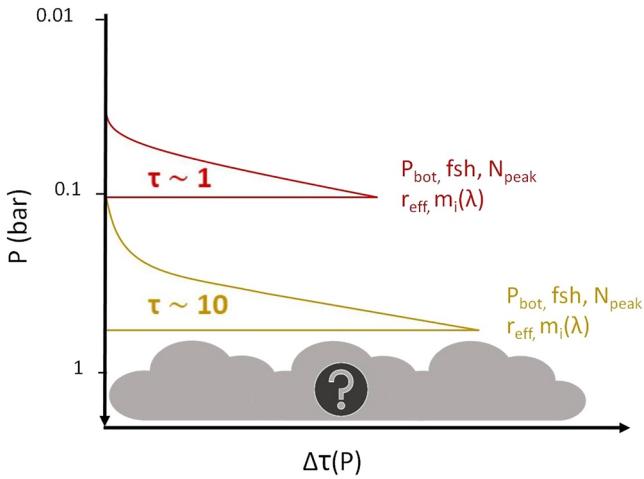

Figure 11. Illustrative sketch of the retrieved cloud structure. The horizontal axis represents the optical depth contribution of each layer and is arbitrarily scaled. We include the free parameters describing the hazes (see Table 3), except for the bottom cloud, since we are insensitive to it (Section 4.4). The actual retrieved parameters describing the atmosphere for each visit and region are shown in Table S1 in Supporting Information S1.

the stratospheric haze, as shown in Table 4. The changes in P($\tau = 1$) shown in Table S1 in Supporting Information S1 are inside the methodological uncertainty, and thus changes in cloud top altitude are not conclusive. The absorbing nature of the hazes does not seem to have changed significantly either, according to the evolution of the imaginary refractive indices shown in Figure 9, which is contrary to the results in Pérez-Hoyos et al. (2009). However, this may be mainly due to the differences between the employed models. Pérez-Hoyos et al. (2009) assumed an optically thin, uncolored stratospheric haze and an extended tropospheric haze from 100–250 down to 700 mbar. As the tropospheric haze in that model is represented as an extended layer of constant concentration, variations in the cloud density would change the haze concentration at all levels, resulting in a massive variation of the total integrated optical thickness of the haze. However, in our model, the stratospheric haze plays the main role in coloration, and, as it is physically thin, small abundance changes are able to account for the observed reflectivity variations without requiring substantial changes in their absorption properties.

The physical mechanism that leads to the color change in the Oval BA annulus is still unknown. A secondary circulation hypothesis that could explain the 2005–2006 reddening was proposed by de Pater et al. (2010b), Wong et al. (2011) and Marcus et al. (2013). In that scenario, the gases ascend and cool in the center of the oval and descend in the red ring. When the gases descend, adiabatic compression leads to a temperature increase that would trigger a temperature-dependent process that leads to the appearance of the chromophore. In particular, they support the "hiding and exposing" mechanism, in which in the white clouds the red particles are coated with white ammonia ice, while the temperature in the ring is high enough to sublimate the ammonia ice and expose the chromophore. Following this scheme, a global climate change resulting in a temperature increase of Oval BA (and at all latitudes north of 34°S) would have been the underlying cause of the 2006 reddening (prior to that increase, the temperature would not have been high enough for the chromophore-exposing process to take place). Pérez-Hoyos et al. (2009) made an extensive analysis of possible causes for the reddening and favored the upwelling of red particles or a colorless material that undergoes chemical/photochemical reactions that lead to a red compound when reaching the upper troposphere. Our results indicate that the color change from red to white was a consequence of a decrease in the stratospheric optical depth, that is, a decrease in the stratospheric chromophore abundance. The chromophore creation and destruction mechanisms proposed in the aforementioned works could account for such decrease. Our results cannot favor any of them on their own, and there is no apparent evidence as to the causes that triggered the color change, necessary to ultimately understand the physical behavior underlying in the Oval BA coloration and possibly in the rest of the Jovian atmosphere.

4.2. GRS: Chromophore Nature and Distribution

We show in Figure 10 the imaginary refractive indices for both the stratospheric and tropospheric hazes and for every observation campaign. No significant changes in the absorbing nature of the hazes can be concluded (i.e., for a given feature, over time, the retrieval results are more or less the same). The pattern appears to be relatively constant and similar to the one presented in A2021: we have two different coloring agents, both showing strong absorption at short wavelengths. The stratospheric haze absorption is stronger than that of the tropospheric haze at wavelengths longer than 300 nm, as the tropospheric haze shows a relatively weak absorption in the visible. This explains why the changes in the tropospheric optical depths for region 9 (Oval BA nucleus) shown in Table 4 are not coupled with a more pronounced color change. Similarly, it is the decrease of the stratospheric optical depth in regions 0 and 1 (GRS nucleus and interior, respectively, see Figure 8) which mostly explains the GRS loss of redness indicated by the RGB images in Figure 3 and the CI curves in Figure 4. However, in region 0, our retrievals suggest a tropospheric haze that is more absorbing than the stratospheric one for $\lambda < 300$ nm. Figure 10 plots seem to point to an absorption band of the stratospheric haze centered at $\lambda \approx 350$ nm. We include in the stratospheric plots of Figure 10 the imaginary refractive index of the chromophore proposed by Carlson et al. (2016) and its slope in the 350–500 nm range. Our retrieved slopes are in reasonable agreement with the

slope of Carlson et al. (2016)'s chromophore. The steepest slopes are found in regions 0 and 1 and fall in the range between $s = -1.88 \cdot 10^{-4}$ nm^{-1} and $s = -1.54 \cdot 10^{-4}$ nm^{-1}. These values are slightly lower than the Carlson et al. value $s = -2.24 \cdot 10^{-4}$ nm^{-1}, which is contrary to the results of Braude et al. (2020). The lower m_i values, however, could be due to the mixture of the chromophore with low-absorbing aerosols in the atmosphere, which increases the scattering and results in a general decrease of the measured absorption, as proposed by A2021. Besides, the Carlson et al. (2016) values were obtained assuming no scattering, and with scattering those values would be reduced, as stated in the supplementary material to that paper.

Our "stratospheric" haze is not fully stratospheric because its base is generally located at 110 mbar, just below the tropopause, but it extends to the stratosphere. We call it "stratospheric" to quickly differentiate it from tropospheric haze. This is important to note when comparing results from other works where their stratospheric haze is located at higher levels in the stratosphere. This is the case for example, of Zhang et al. (2013) and López-Puertas et al. (2018), with both works showing equatorial stratospheric hazes located at ∼50 mbar and with optical depths of the order of the hundredth. We could also consider these hazes in our model, as their low optical depths would contribute slightly to the overall extinction, but it would increase the number of free parameters and thus decrease the statistical significance of the fits. Another interesting case is given in Braude et al. (2020), where they show for the GRS a light stratospheric haze above 150 mbar and a chromophore layer located near 200 mbar. Our stratospheric haze would be the analog to their chromophore layer, rather than their stratospheric haze. In fact, we obtain a similar overall scheme to some extent if we consider that the chromophore layer is located near the top of a denser tropospheric cloud. The cloud's absorption spectra are not wavelength-dependent in Braude et al. (2020), but that is also what we get for their spectral range (480–930 nm). However, for the GRS, we retrieve peak optical depths per bar that are approximately 40 times the one presented in that work for their preferred model, although they also show retrievals with similar low χ^2/N values in which this difference is reduced to a factor ∼3. This may be due to our lower imaginary refractive indices, which require higher chromophore abundances. Another difference is that Braude et al. (2020) locate their chromophore layer and tropospheric cloud peak density near the 200 mbar level, that is, their chromophore/tropospheric layer is located lower/higher than our retrieved ones. This could be due to their lack of UV data below 480 nm, which adds sensitivity to the stratospheric levels.

We show in Figure 11 a schematic representation of the retrieved atmospheric layout. The vertical distribution of the stratospheric chromophore remains qualitatively unchanged and on an intermediate level between the "Crème-Brûlée" model (Baines et al., 2019; Sromovsky et al., 2017) and an extended chromophore scheme (Pérez-Hoyos et al., 2020), as also explained by A2021. It should also be noted that the curve given by Carlson et al. (2016) is very absorbing, and so models employing those values need to locate the chromophore in a very thin layer with optical depths generally of the order of 0.1 ("Crème-Brûlée" model), while for our blue-absorbing stratospheric haze we obtain optical depths generally of the order of 1. Since we use a more extended chromophore layer, lower imaginary refractive index values and higher optical depths are to be expected just by model construction.

The altitude difference of the Carlson-colored layers ($P_{bot} \sim 200$ mbar) in works using the "Crème-Brûlée" scheme (Baines et al., 2019; Sromovsky et al., 2017) and our stratospheric haze ($P_{bot} \sim 100$ mbar), while not substantial, is not negligible. Its cause might be the contribution of the UV filters used in this work, whose wavelengths are not covered by Cassini/VIMS and are sensitive to the contributions from the submicron sized aerosols at the upper tens of mbar of the atmosphere (Pérez-Hoyos et al., 2020).

To check the performance of the "Crème-Brûlée" scheme on our data, we conducted tests using such scheme as in Pérez-Hoyos et al. (2020) on regions 0 (GRS nucleus) and 5 (STrZ) for visit "OPAL 2017," which is our data set with best observational constraints. For that purpose, we use the imaginary refractive index curve of Carlson et al. (2016) extrapolated to wavelengths shorter than 400 nm as in Fry and Sromovsky (2023). When setting the imaginary refractive indices as fixed parameters, we retrieved $\tau_{chromophore}$ (900 nm) = 0.14 ± 0.04 and χ^2/N = 4.16 for the GRS nucleus, and $\tau_{chromophore}$ (900 nm) = 0.12 ± 0.05 and χ^2/N = 1.8 for the STrZ. Better results were obtained when we let $m_i(\lambda) < 400$ nm vary as a free parameter, which led to $\tau_{chromophore}$ (900 nm) = 0.16 ± 0.05 and χ^2/N = 1.26 and $\tau_{chromophore}$ (900 nm) = 0.14 ± 0.06 and χ^2/N = 1.30 for the GRS nucleus and the STrZ, respectively. Although our model showed a better overall performance for these regions both in terms of spectral and limb-darkening fitting, it is noteworthy that the $m_i(\lambda)$ values were decreased for $\lambda < 350$ nm and increased at $\lambda \approx 350$ nm for both the GRS and the STrZ, which again points to the presence of the absorption band centered at $\lambda \approx 350$ nm shown in Figure 10.

A remarkable fact when comparing our model to the "Crème-Brûlée" scheme is that we are not sensitive to the bottom cloud while previous investigations have shown that the visual spectrum accesses Jupiter down to one bar

Table 5
Retrieved Parameters Using the "Crème-Brûlée" Scheme on "OPAL 2017" Data

	Fixed $m_i(\lambda) < 400$ nm				Variable $m_i(\lambda) < 400$ nm			
	τ_{chromo} (900 nm)	r_{chromo} (μm)	P_{bot} (mbar)	χ^2/N	τ_{chromo} (900 nm)	r_{chromo} (μm)	P_{bot} (mbar)	χ^2/N
Region 0 GRS nucleus	0.14 ± 0.04	0.08 ± 0.02	110 ± 10	4.16	0.16 ± 0.05	0.08 ± 0.02	80 ± 20	1.26
Region 5 STrZ	0.12 ± 0.05	0.19 ± 0.07	350 ± 60	1.80	0.14 ± 0.06	0.20 ± 0.05	320 ± 60	1.30

or more (e.g., Baines et al., 2019; Sromovsky et al., 2017). But, in fact, we are sensitive to a comparable amount of light extinction. The "Crème-Brûlée" scheme has optically thin layers ($\tau \sim 0.1$) above the main tropospheric cloud ($\tau \sim 10$), while we have a stratospheric haze with $\tau \sim 1$ and a tropospheric haze with $\tau \sim 10$. Thus, we obtain similar optical depths, but our research shows a preference for the model with a high opacity haze at higher tropospheric levels.

We tried the "Crème-Brûlée" layout on our data and found that it works reasonably well. In this case, we are sensitive to the bottom cloud, with $\tau_{cloud} \approx 20$ (similarly to Fry and Sromovsky (2023), for the North Equatorial Belt). However, our model shows better fits to the observed spectral and limb-darkening behavior. We also conducted experiments reducing the opacity of the stratospheric and tropospheric hazes in our model. For the best fit in the GRS nucleus in visit "OPAL 2017," we retrieved stratospheric and tropospheric haze optical depths about 10 times lower ($\tau_{str} = 0.25$ and $\tau_{trop} = 3.85$) and a bottom cloud optical depth of $\tau_{cloud} = 13$. The reduced haze opacity allows to be sensitive to the bottom cloud, but the resulting fit of the data was substantially worse with $\chi^2/N = 2.35$. Tests with more cloud opacity led to even worse fits.

We show in Table 5 the retrieved optical depths, bottom pressures and mean effective radii of the chromophore layer for the "Crème-Brûlée" layout. The top pressure of the chromophore layer is equal to 0.9 times the base pressure.

4.3. Altitude and Particle Size

As stated in Section 2.5, the spectral clustering allows the extrapolation of the retrieved properties of the analyzed regions to other areas of the map with similar spectra belonging to the same cluster, at least as a first approximation. An example of this application is shown in Figures 12 and 13, where maps of cloud top effective altitudes and mean tropospheric radii are shown, respectively.

Figure 12 shows the high temporal and spatial variability of the studied area. The GRS interior values are the average of values corresponding to regions 0 and 1 (GRS nucleus and interior, respectively), as they fall in the same spectral cluster. As expected from the AOI maps in Figure S2 in Supporting Information S1, the cloud top altitude maps show that the GRS is located higher in the atmosphere than its surroundings. The area northwest of the GRS with vertically extended convective clouds (Sánchez-Lavega et al., 2008) is highly variable, as the latitudinal wind shear makes them disappear in a time scale of few days (Hueso et al., 2002). The deepest region in the studied extent is the STrZ. Oval BA has a higher cloud top than its surroundings, in agreement with previous works (Banfield et al., 1998; Pérez-Hoyos et al., 2009). The oval shows a little decrease in altitude from 2016 to 2020. However, as aforementioned in Section 4.1, the change in altitude is inside the methodological uncertainty and thus we cannot conclude a general altitude decrease in the oval, which is in agreement with prior results regarding the 2005–2006 reddening (Pérez-Hoyos et al., 2009; Wong et al., 2011). This is also clear from the errors in the $P(\tau = 1)$ values in Table S1 in Supporting Information S1. However, regarding these errors, it should be noted that, in general terms, uncertainty increases as penetration depth gets bigger, except for cases with high optical thickness of the stratospheric haze. This is due to the fact that altimetry is governed mainly by deep methane band filter (FQ889N) and, to a lesser extent, by ultraviolet filters and intermediate methane band filter (FQ727N) which are most sensitive to the upper tropospheric levels (de Pater et al., 2010a).

The maps of mean tropospheric radii in Figure 13 show a particle size increase in the GRS interior in 2018. The reader should note again that the GRS interior values are the average of regions 0 and 1. This is important because the mean tropospheric radius in region 1 is quite constant around the 0.8 μm value, while we get bigger values for region 0, as well as larger variations among different years. Similarly, we also get higher radii in the Oval BA nucleus than in the ring and periphery (see Table S1 in Supporting Information S1). Therefore, this seems to be a

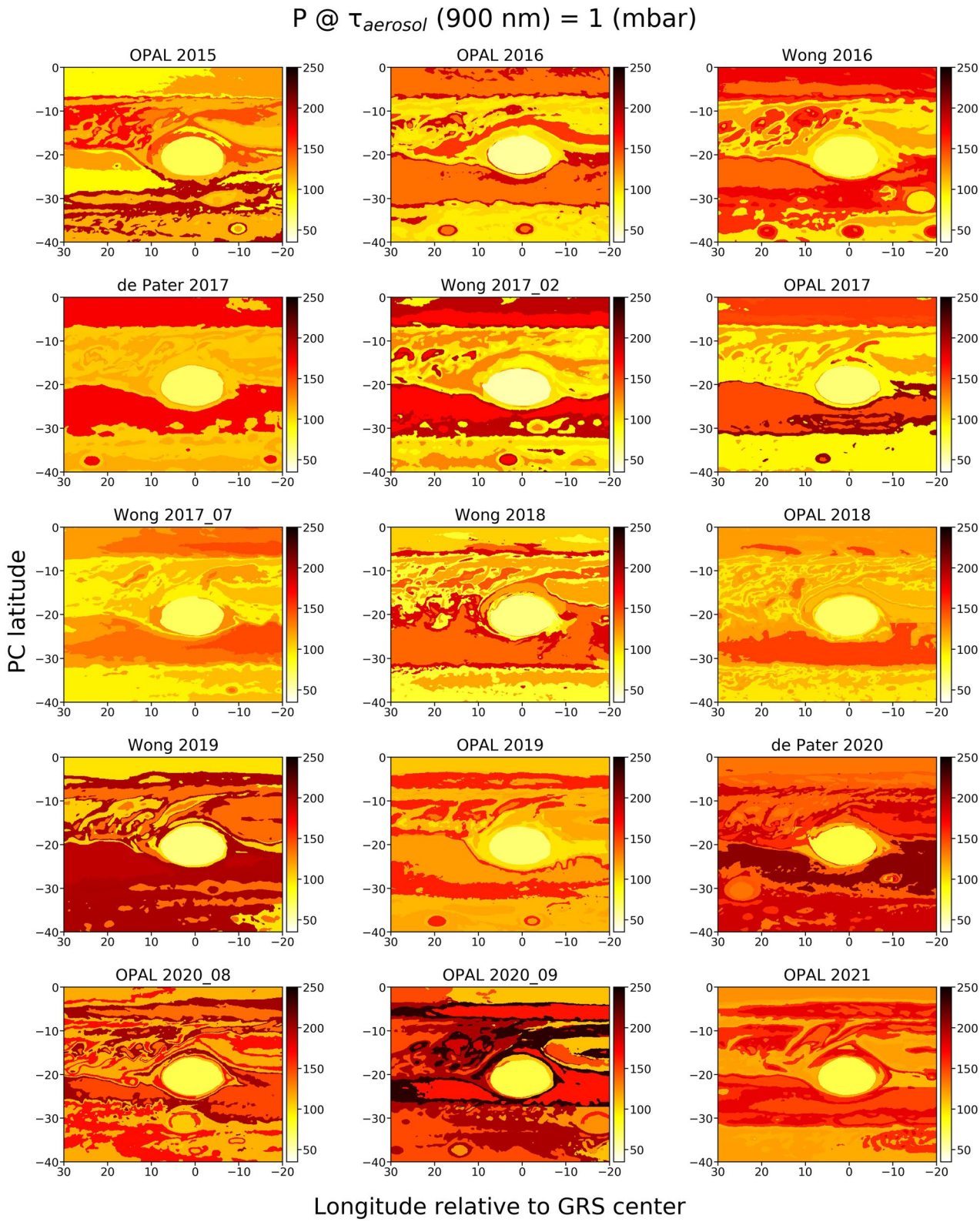

Figure 12. Maps showing the pressure levels where the optical depth at 900 nm equals unity. This magnitude is interpreted as the cloud top effective altitude. Visit "de Pater 2018" is not included for graphic purposes. The maps for all visits are available at the companion repository of this paper (Anguiano-Arteaga et al., 2023).

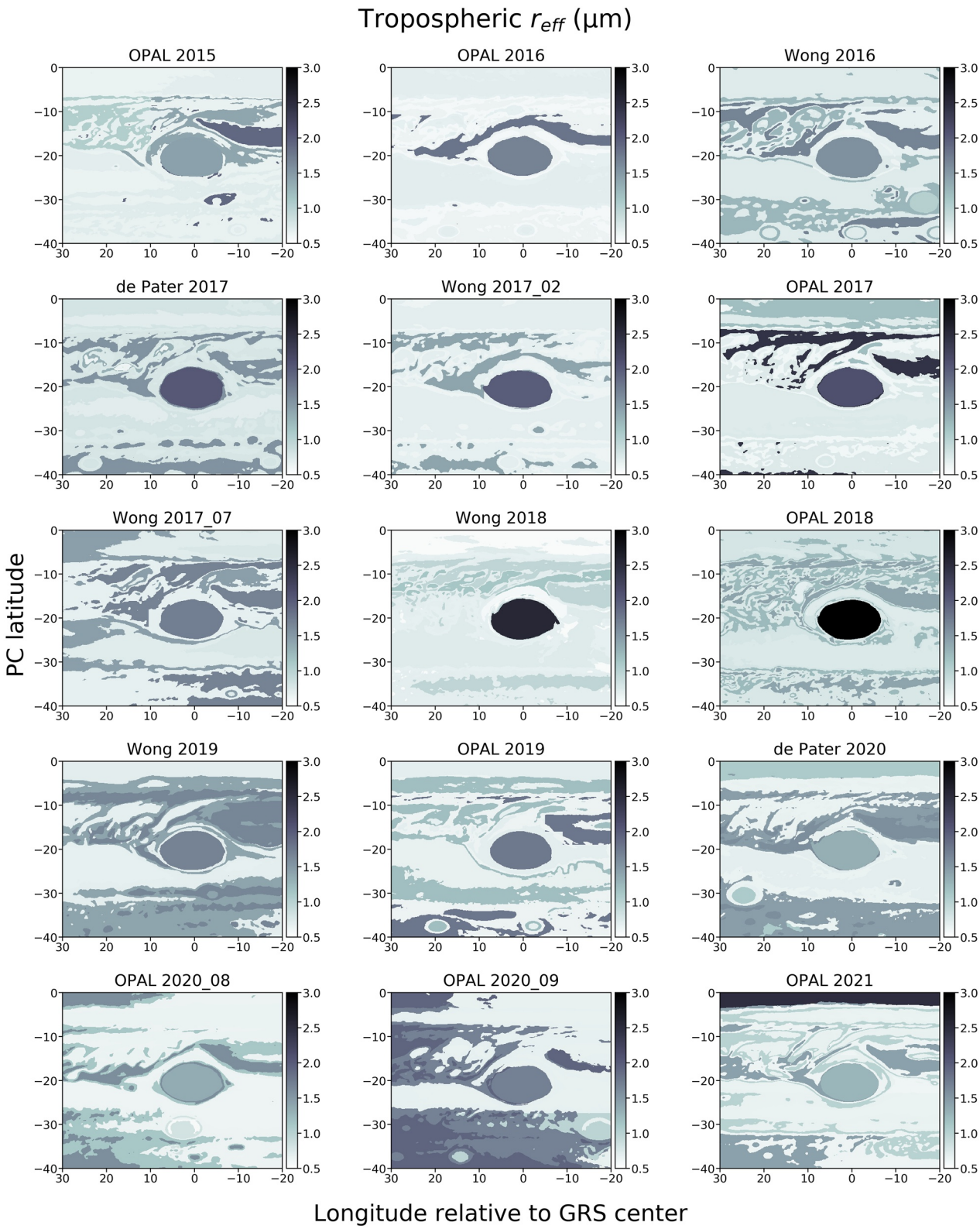

Figure 13. Maps showing the mean effective radii of the tropospheric particle size distribution. Visit "de Pater 2018" is not included for graphic purposes. The maps for all visits are available at the companion repository of this paper (Anguiano-Arteaga et al., 2023).

feature shared at least by the biggest Jovian anticyclones. At the same time, the STrZ, the "hollow" and the area of intense convective activity northwest of the GRS show the tiniest particles, with radii in the 0.5–0.8 μm range. However, the STrZ shows important morphological changes that are coupled with changes in the particle size distribution. On the other hand, the low-albedo clouds in the westward jet located approximately at 20°S carry big particles when compared to the rest of the GRS surroundings. The EZ shows a relevant increase in the mean particle size in 2021, possibly related to its color change.

We do not include maps of the mean stratospheric particle radii because they are almost constant with tiny oscillations around the 0.3 μm mean value. This is quite compatible with the $r_{\text{eff}} = 0.1$–0.2 μm values given by Sromovsky et al. (2017) and Baines et al. (2019) in their application of the Carlson et al. (2016) chromophore to different Jovian areas.

4.4. Sensitivity Analysis

In this section we analyze the response of our model to variations in the value of retrieved parameters (see Tables 3 and Table S1 in Supporting Information S1). More specifically, we show the effect on the output spectra of increasing and decreasing each retrieved free parameter by 50%, similar to the work by Dahl et al. (2021). Although a more in-depth analysis would be desirable to cover all mutual correlations among parameters, given the high dimensionality of the free parameter space, this is a good way to understand the limitation of the retrievals. We performed this analysis on the GRS nucleus (region 0) and the STrZ (region 5), as these regions are very different both from a dynamical and spectral point of view, and thus allow us to compare the response of parameter variations on different atmospheric layouts. We only show this analysis for visits "Wong 2016" and "OPAL 2017." These were chosen because of the number of viewing geometries (3 and 4, respectively).

Figure 14 shows the percentage difference in *I*/*F* resulting from increasing (solid lines) and decreasing (dashed lines) each parameter by 50% with respect to the reference value. In the case of the bottom pressure of the hazes, we varied the bottom height and then translated it into pressures, since heights are the input to NEMESIS. The figure corresponds to visit "Wong 2016" and the analysis is performed on region 0 (GRS nucleus). Analogous figures for the other cases (region 5 in "Wong 2016" and regions 0 and 5 in "OPAL 2017") can be found in Figures S4–S6 in Supporting Information S1. We only compare here two viewing geometries for clarity: in the first one, the GRS is centered at 60°W (blue lines) and in the other at 15°E (red lines).

It can be seen from Figure 14 that an increase of the stratospheric haze bottom pressure (or a decrease of the bottom altitude, which is the actual NEMESIS input) leads to a decrease of UV reflectivity. This may be counter-intuitive, since lowering the haze would enhance the Rayleigh back scattering and increase the observed reflectivity. However, lowering the base altitude of the stratospheric haze leads to an overlap between the stratospheric and tropospheric haze particles. Since the tropospheric haze particles are stronger UV absorbers, as shown in Section 4.2, this leads to them interacting more directly with the incoming sunlight and thus lowering the overall reflectivity. There is also a reflectivity increase in the visible for very similar reasons, as the tropospheric haze particles are better scatterers (a larger particle size implies a larger cross-section). Increasing the stratospheric haze bottom pressure also reduces reflectivity in filter FQ889N because the incoming light travels a longer path and therefore undergoes more CH_4 absorption. The opposite happens with a decrease in the stratospheric bottom pressure, although in this case changes in the visible do not exceed 5%. Although filter FQ727N also covers a CH_4 band, its reflectivity behavior is opposite to that of FQ889N. This is mainly due to the difference in methane absorption and thus in sounding levels. The increase of the stratospheric haze bottom pressure leads to the exposure of the more strongly scattering tropospheric particles, which in turn increases the observed reflectivity. It should also be noted that differences between the red and the blue lines indicate different levels of sensitivity depending on the viewing geometry of the target.

Elevating the bottom of the tropospheric haze makes the atmospheric path shorter and thus there is lesser Rayleigh-back-scattered light, which only contributes significantly at short wavelengths, reducing the UV reflectivity. The shorter atmospheric path also explains the *I*/*F* increase in filter FQ889N. Changes in the visible are more significant in filter FQ727N, and increasing the tropospheric haze bottom pressure leads to an opposite overall behavior but of a lower magnitude and without distinction between viewing geometries (i.e., no limb-darkening effect). It is also worth noting that the effect of varying the tropospheric haze bottom pressure is very similar to varying its fractional scale height, and maybe this has an effect on constraining the tropospheric

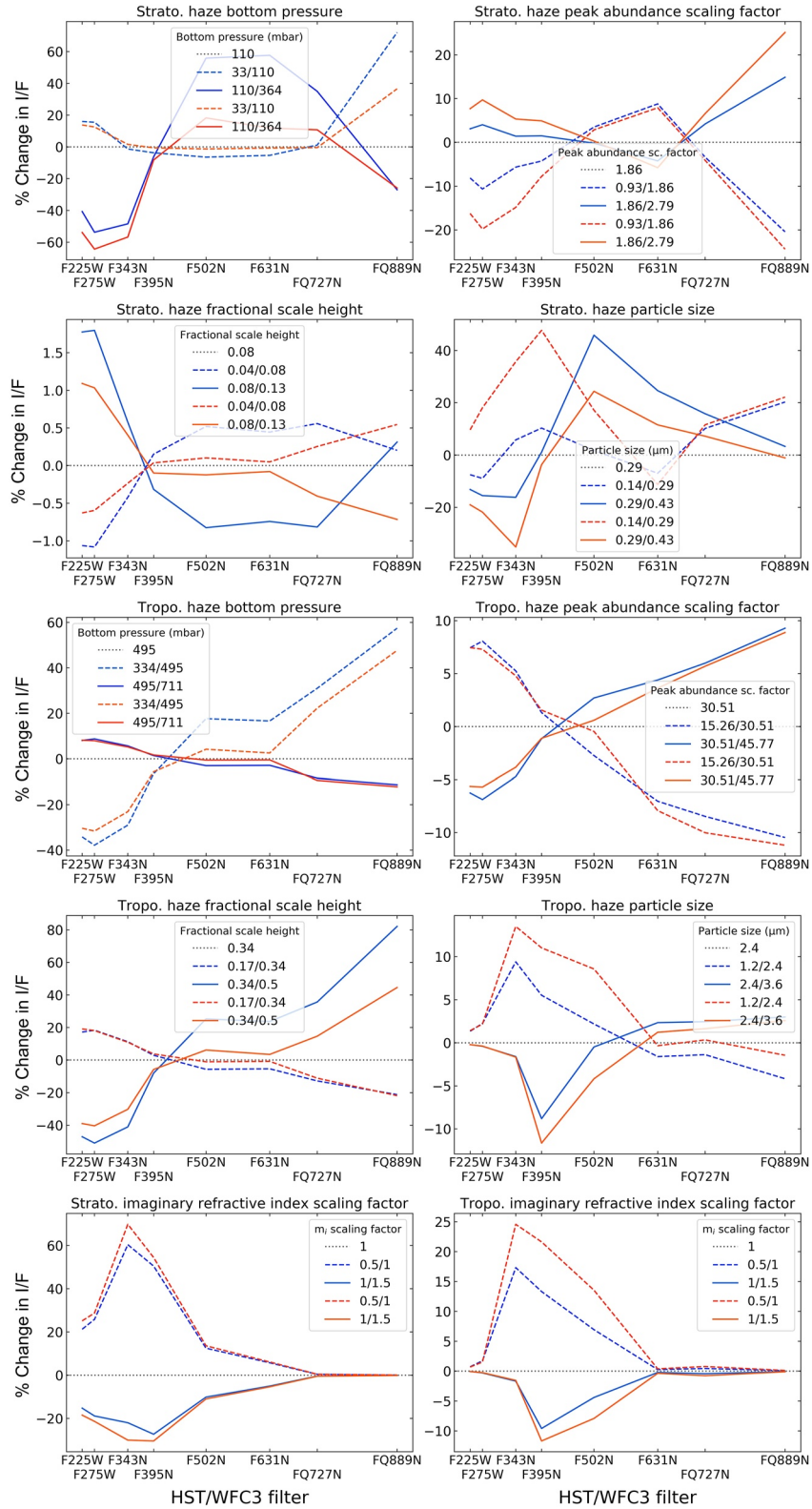

Figure 14. Difference in "Wong 2016" Great Red Spot of Jupiter (GRS) nucleus spectra resulting from increasing (continuous lines) and decreasing (dotted lines) each parameter by 50% with respect to the original retrieved value. For the bottom pressures, we varied the bottom height and then translated it into pressure. The blue and red lines correspond to viewing geometries with the GRS nucleus located at 60°W and 15°E, respectively. Black dotted lines indicate the retrieved parameter values.

haze bottom pressure (see Section 3.2). However, varying these parameters induces some *I*/*F* changes in filters F225W, F275W and FQ889N when the target is near limb and in filter FQ727N for both geometries. On the other hand, varying the stratospheric haze fractional scale height produces minor changes (lower than 2%).

The peak abundance of the stratospheric haze is an input parameter to NEMESIS that scales the maximum haze abundance reached at bottom pressure, with units of haze particles per gram of atmosphere. Figure 14 shows that varying it leads to larger differences when the target is close to the CM. At the same time, changes are more pronounced in filters F225W, F275W, and FQ889N. The case of varying the peak abundance of the tropospheric haze induces lower changes, and there is little distinction between viewing geometries. The most significant changes, however, again take place in filters F225W, F275W, and FQ889N, indicating that these filters are not sensitive only to the altitude of the hazes but also to their optical depths.

The case of varying the stratospheric particle size is a bit more complex. Such changes induce variations in the cross-sections as a function of wavelength, potentially shifting the maximum, depending on the size-to-wavelength ratio. When the particle size is increased and the target is close to the CM, the largest changes occur in filter F343N. This is again due to the absorption peak of the haze at that wavelength (Section 4.2). Nevertheless, when the particle size is decreased, the maximum effect is in filter F395N, which has the second highest absorption. When the target is close to the limb and the particle size is decreased, there is also a peak in F395N, although larger differences are found in FQ889N. Except in this case, the largest differences take place in intermediate filters and not in filters F225W, F275W, and FQ889N. On the other hand, varying the tropospheric haze particle size induces distinguishable changes between different viewing geometries, and we again find peaks in filters F343N and F395N. However, the effect of varying the tropospheric particle size is much lower, with maximum variations close to 10%.

Differences when varying the imaginary refractive indices of the stratospheric and tropospheric hazes also show peaks in filters F343N and F395N. However, these changes are more significant for the stratospheric haze since it is a more powerful absorber (it has higher imaginary refractive indices, see Section 4.2). In addition, the stratospheric haze shows little distinction between different viewing geometries, and no changes are found in the longest wavelengths. For the tropospheric haze, decreasing the imaginary refractive indices induces more distinguishable differences when the target is close to the CM, when penetration depth is probably the highest, and negligible changes are found in filters F225W, F275W, F631N, FQ727N, and FQ889N. It should be noted that for the sensitivity analysis we change the imaginary refractive indices by multiplying the retrieved curves by a scaling factor in order to more compactly analyze the effect of variations at all wavelengths simultaneously, although the imaginary refractive indices are fitted at each wavelength and not scaling a predefined curve.

As stated in Section 3.1, we do not include in Table 3 the parameters describing the bottom ammonia cloud because we are not sensitive to it. In order to analyze the sensitivity of our model to the bottom cloud, we have calculated the difference in *I*/*F* between our nominal model ($\tau_{\text{cloud}} \approx 0$) and two extreme cases in which we have $\tau_{\text{cloud}} = 10$ and $\tau_{\text{cloud}} = 100$. The difference in *I*/*F* for such drastically different clouds is never above 2% in any of the used filters (see Figure S7 in Supporting Information S1), and therefore we conclude that we are not sensitive to a potential bottom cloud deck.

In summary, this preliminary analysis shows the complex relation between parameters, viewing geometries and filters. It is far beyond the scope of this paper to analyze these relationships in more detail as it would require enormous amounts of computing time. However, some important aspects stand out even from a preliminary analysis. The selected free parameters have a clear effect on the observed reflectivity, while the bottom cloud has a negligible effect on our retrievals, thus supporting our approach to the problem.

5. Conclusions

We have shown in this work the evolution of color and relevant aerosol properties for the GRS, its rich dynamical surroundings and Oval BA from 2015 to 2021. We have used HST/WFC3 images covering from the UV (225) to the near-IR (900 nm) and selected for further analysis 13 different regions according to their morphological and spectral features. For each selected region, we use as a priori model atmosphere the retrieved one for the analogous region in visit "Wong 2016." These models were the outcome of an extensive analysis focusing on the fitting of measured spectral and limb-darkening curves (A2021). More specifically, almost 12,000 different models were explored by analyzing the fits of spectra corresponding to five regions along different longitudes in the STrZ. The

application of the "Wong 2016" models to other years' spectra has been successful, proving its consistency. In the following, we summarize our main conclusions.

- Although they are allowed to vary as free parameters, all the retrieved models for all the regions analyzed share the following: a stratospheric haze with its base near 110 mbar with r_{eff}~≈ 0.3 μm, $\tau \sim 1$ and an optically thick (τ down to 330 mbar in the 1–25 range) tropospheric haze based at 500 mbar with mean particle size in the 0.5–6 μm range. We are not sensitive to deeper pressure levels. Our retrieved tropospheric hazes have accumulated optical depths of the order of 10, and thus our models assume that most of the light extinction in our studied wavelengths occurs at higher levels than 500 mbar. Both hazes have a wavelength-dependent imaginary refractive index, contributing to the coloration of the analyzed regions, with no major temporal variations found. The stratospheric imaginary refractive index curves might be compatible with the chromophore proposed by Carlson et al. (2016). A possible explanation for the lower values found here is the mixture of the chromophore with non-absorbing material present in stratospheric levels. Furthermore, the variations of the stratospheric and tropospheric imaginary refractive indices among the different regions could also be explained by various degrees of abundance and mixing with non-absorbing compounds. If this were true, it would support the universal chromophore scheme proposed by Sromovsky et al. (2017), but with the addition of a new coloring species at tropospheric levels. Laboratory work testing plausible compounds on the UV regime would be needed to test this hypothesis.
- We find a decrease in the stratospheric and tropospheric optical depths inside the GRS red oval (regions 0 and 1), starting in 2019 (see Figure 8). The change between 2018 and 2020 in stratospheric haze optical depth is about 10% and 30% for regions 0 (GRS nucleus) and 1 (GRS interior), respectively. For the tropospheric haze optical depth, the decrease is approximately 50% and 40% for those regions. This seems to explain the decreasing altitude/opacity and redness indicated by the AOI and CI temporal curves, respectively (see Figure 4). However, the optical depths for both the stratospheric and tropospheric haze seem to increase again in 2021, although more data would be suitable to support this. The cause of these variations is beyond the scope of this paper, but the interactions of the GRS with smaller anticyclones starting in 2019 (Sánchez-Lavega et al., 2021) may be somehow related to this phenomenon. In seems likely that a vortex circulation model including secondary circulation and coupled to a microphysical model would be needed to unveil the origin of the color changes. We also find a notable increase in the mean tropospheric particle size in region 0 in year 2018 (see Figure 13), where this value increases from 2-3 to 4–6 μm. The tropospheric particle size in the GRS nucleus is found to be larger than in the rest of its reddish interior area, with the mean radius in region 1 being approximately 35% of the region 0 particle mean radius (without considering the larger radii found in 2018).
- Our model explains the color change from reddish to white undergone by Oval BA in terms of a decrease in the stratospheric optical depth. The biggest decrease occurs in region 11 (the ring surrounding the nucleus that changed from red to white), with a decrease of 35%. We also find a decrease of 12.5% and 10% in the stratospheric optical thickness of the oval nucleus and the periphery of white clouds, respectively. Regarding the tropospheric optical haze, we find a decrease of 40% in region 9 (nucleus), a 20% increase in region 10 (periphery) and practically no change in region 11 (inner ring). This result is not in agreement with the findings of previous works studying the 2005–2006 color change (Pérez-Hoyos et al., 2009; Simon-Miller et al., 2006; Wong et al., 2011). As in the GRS, we find larger tropospheric particle radii in the nucleus of the oval than in the surrounding areas, with a mean particle size nearly doubling the values found in regions 10 and 11.

We have shown the temporal evolution of several regions in the GRS, its surroundings and Oval BA. The causes of the presented changes remain unclear and its relation to dynamical aspects is still a big unknown, as the nature and origin of the Jovian chromophores remains an unanswered question. However, we here encourage the study of these chromophores, particularly the one proposed by Carlson et al. (2016), as it provides a comprehensive scheme which seems able to explain observations in a wide range of wavelengths for a number of dynamically diverse regions experiencing very intense morphological and color changes.

Data Availability Statement

Repository with the data of the figures shown in the main text and supplementary information: Anguiano-Arteaga et al. (2023).
NEMESIS/Radiative transfer code software: Irwin (2022).

The HST images used in this work are publicly available at the Mikulski Archive for Space Telescopes, managed by the Space Telescope Science Institute.

Acknowledgments
This work has been supported by the Spanish project PID2019-109467GB-I00 (MINECO/FEDER, UE) and Grupos Gobierno Vasco IT1366-19. This work used data acquired from the NASA/ESA HST Space Telescope, archived at the Space Telescope Science Institute, which is operated by the Association of Universities for Research in Astronomy, Inc., under NASA Contract NAS 5-26555.

References

Anguiano-Arteaga, A., Pérez-Hoyos, S., Sánchez-Lavega, A., Sanz-Requena, J. F., & Irwin, P. G. J. (2021). Vertical distribution of aerosols and hazes over Jupiter's Great Red Spot and its surroundings in 2016 from HST/WFC3 imaging. *Journal of Geophysical Research: Planets*, *126*, e2021JE006996. https://doi.org/10.1029/2021JE006996

Anguiano-Arteaga, A., Pérez-Hoyos, S., Sánchez-Lavega, A., Sanz-Requena, J. F., & Irwin, P. G. J. (2023). DATA REPOSITORY: Temporal variations in vertical cloud structure of Jupiter's Great Red Spot, its surroundings and oval BA from HST/WFC3 imaging [Dataset]. Zenodo. https://doi.org/10.5281/zenodo.8124154

Asay-Davis, X., Marcus, P. S., Wong, M. H., & de Pater, I. (2009). Jupiter's shrinking Great Red Spot and steady Oval BA: Velocity measurements with the 'Advection corrected correlation image velocimetry' automated cloud-tracking method. *Icarus*, *203*, 164–188. https://doi.org/10.1016/j.icarus.2009.05.001

Baines, K. H., Sromovsky, L. A., Carlson, R. W., Momary, T. W., & Fry, P. M. (2019). The visual spectrum of Jupiter's Great Red Spot accurately modeled with aerosols produced by photolyzed ammonia reacting with acetylene. *Icarus*, *330*, 217–229. https://doi.org/10.1016/j.icarus.2019.04.008

Banfield, D., Gierasch, P. J., Bell, M., Ustinov, E., Ingersoll, A. P., Vasavada, A. R., et al. (1998). Jupiter's cloud structure from Galileo imaging data. *Icarus*, *135*, 230–250. https://doi.org/10.1006/icar.1998.5985

Braude, A. S., Irwin, P. G. J., Orton, G. S., & Fletcher, L. N. (2020). Colour and tropospheric cloud structure of Jupiter from MUSE/VLT: Retrieving a universal chromophore. *Icarus*, *338*, 113589. https://doi.org/10.1016/j.icarus.2019.113589

Calamida, A., Mack, J., Medina, J., Shahanan, C., Bajaj, V., & Deustua, S. (2021). New time-dependent WFC3 UVIS inverse sensitivities. STScI, WFC3 Instrument Science Report 2021-04.

Carlson, R. W., Baines, K. H., Anderson, M. S., Filacchione, G., & Simon, A. A. (2016). Chromophores from photolyzed ammonia reacting with acetylene: Application to Jupiter's Great Red Spot. *Icarus*, *274*, 106–115. https://doi.org/10.1016/j.icarus.2016.03.008

Cheng, A. F., Simon-Miller, A. A., Weaver, H. A., Baines, K. H., Orton, G. S., Yanamandra-Fisher, P. A., et al. (2008). Changing characteristics of Jupiter's little red spot. *The Astronomical Journal*, *135*, 2446–2452. https://doi.org/10.1088/0004-6256/135/6/2446

Dahl, E. K., Chanover, N. J., Orton, G. S., Baines, K. H., Sinclair, J. A., Voelz, D. G., et al. (2021). Vertical structure and color of Jovian latitudinal cloud bands during the Juno era. *The Planetary Science Journal*, *2*, 16. https://doi.org/10.3847/PSJ/abd400

de Pater, I., Fletcher, L. N., Pérez-Hoyos, S., Hammel, H. B., Orton, G. S., Wong, M. H., et al. (2010a). A multi-wavelength study of the 2009 impact on Jupiter: Comparison of high resolution images from Gemini, Keck and HST. *Icarus*, *210*, 722–741. https://doi.org/10.1016/j.icarus.2010.07.010

de Pater, I., Wong, M. H., Marcus, P. S., Luszcz-Cook, S., Ádámkovics, M., Conrad, A., et al. (2010b). Persistent rings in and around Jupiter's anticyclones - Observations and theory. *Icarus*, *210*, 742–762. https://doi.org/10.1016/j.icarus.2010.07.027

Dressel, L. (2021). *Wide Field Camera 3 instrument handbook, version 13.0*. STScI.

Fry, P. M., & Sromovsky, L. A. (2023). Investigating temporal changes in Jupiter's aerosol structure with rotationally-averaged 2015–2020 HST WFC3 images. *Icarus*, *389*, 115224. https://doi.org/10.1016/j.icarus.2022.115224

García-Melendo, E., Legarreta, J., Sánchez-Lavega, A., Hueso, R., Pérez-Hoyos, S., Gómez-Forrellad, J. M., et al. (2009). The Jovian anticyclone BA: I. Motions and interaction with the GRS from observations and non-linear simulations. *Icarus*, *203*, 486–498. https://doi.org/10.1016/j.icarus.2009.05.031

Hueso, R., Legarreta, J., García-Melendo, E., Sánchez-Lavega, A., & Pérez-Hoyos, S. (2009). The Jovian anticyclone BA: II. Circulation and interaction with the zonal jets. *Icarus*, *203*, 499–515. https://doi.org/10.1016/j.icarus.2009.05.004

Hueso, R., Sánchez-Lavega, A., & Guillot, T. (2002). A model for large-scale convective storms in Jupiter. *Journal of Geophysical Research*, *107*, 5075. https://doi.org/10.1029/2001JE001839

Irwin, P. G. J., Bowles, N., Braude, A. S., Garland, R., Calcutt, S., Coles, P. A., et al. (2019). Analysis of gaseous ammonia (NH_3) absorption in the visible spectrum of Jupiter – Update. *Icarus*, *321*, 572–582. https://doi.org/10.1016/j.icarus.2018.12.008

Irwin, P. G. J., Teanby, N. A., de Kok, R., Fletcher, L. N., Howett, C. J. A., Tsang, C. C. C., et al. (2008). The NEMESIS planetary atmosphere radiative transfer and retrieval tool. *Journal of Quantitative Spectroscopy and Radiative Transfer*, *109*, 1136–1150. https://doi.org/10.1016/j.jqsrt.2007.11.006

Irwin, P. G. J., Teanby, N. A., de Kok, R., Fletcher, L. N., Howett, C. J. A., Tsang, C. C. C., et al. (2022). Nemesis [Software]. Zenodo. https://doi.org/10.5281/zenodo.5816714

Jancey, R. C. (1966). Multidimensional group analysis. *Australian Journal of Botany*, *14*, 127–130. https://doi.org/10.1111/j.1467-9450.1973.tb00104.x

Karkoschka, E. (1998). Methane, ammonia, and temperature measurements of the Jovian planets and Titan from CCD–spectrophotometry. *Icarus*, *133*, 134–146. https://doi.org/10.1006/icar.1998.5913

Loeffler, M. J., Hudson, R. L., Chanover, N. J., & Simon, A. A. (2016). The spectrum of Jupiter's Great Red Spot: The case for ammonium hydrosulfide (NH_4SH). *Icarus*, *271*, 265–268. https://doi.org/10.1016/j.icarus.2016.02.010

López-Puertas, M., Montañés-Rodríguez, P., Pallé, E., Sánchez-López, A., García-Comas, M., & Funke, B. (2018). Aerosols and water ice in Jupiter's stratosphere from UV-NIR ground-based observations. *The Astronomical Journal*, *156*(4), 169. https://doi.org/10.3847/1538-3881/aadcef

Marcus, P. S., Asay-Davis, X., Wong, M. H., & de Pater, I. (2013). Jupiter's red oval BA: Dynamics, color, and relationship to Jovian climate change. *Journal of Heat Transfer*, *135*, 011007. https://doi.org/10.1115/1.4007666

McLean, W., Stam, D. M., Bagnulo, S., Borisov, G., Devogèle, M., Cellino, A., et al. (2017). A polarimetric investigation of Jupiter: Disk-resolved imaging polarimetry and spectropolarimetry. *Astronomy & Astrophysics*, *601*, A142. https://doi.org/10.1051/0004-6361/201629314

Ordonez-Etxeberria, I., Hueso, R., Sánchez-Lavega, A., & Pérez-Hoyos, P. (2016). Spatial distribution of Jovian clouds, hazes and colors from Cassini ISS multi-spectral images. *Icarus*, *267*, 34–50. https://doi.org/10.1016/j.icarus.2015.12.008

Pérez-Hoyos, S., Sánchez-Lavega, A., Hueso, R., García-Melendo, E., & Legarreta, J. (2009). The Jovian anticyclone BA: III. Aerosol properties and colour change. *Icarus*, *203*, 516–530. https://doi.org/10.1016/j.icarus.2009.06.024

Pérez-Hoyos, S., Sánchez-Lavega, A., Sanz-Requena, J. F., Barrado-Izagirre, N., Carrión-González, O., Anguiano-Arteaga, A., et al. (2020). Color and aerosol changes in Jupiter after a North temperate belt disturbance. *Icarus*, *132*, 114021. https://doi.org/10.1016/j.icarus.2020.114031

Pérez-Hoyos, S., Sanz-Requena, J. F., Barrado-Izagirre, N., Rojas, J. F., Sánchez-Lavega, A., & The IOPW Team. (2012a). The 2009-2010 fade of Jupiter's South Equatorial Belt: Vertical cloud structure models and zonal winds from visible imaging. *Icarus*, *217*, 256–271. https://doi.org/10.1016/j.icarus.2011.11.008

Pérez-Hoyos, S., Sanz-Requena, J. F., Sánchez-Lavega, A., Wong, M. H., Hammel, H. B., Orton, G. S., et al. (2012b). Vertical cloud structure of the 2009 Jupiter impact based on HST/WFC3 observations. *Icarus*, *221*, 1061–1078. https://doi.org/10.1016/j.icarus.2012.10.012

Rogers, J. H. (1995). *The giant planet Jupiter* (p. 45). Cambridge University Press.

Rogers, J. H. (2019). *Jupiter in 2019, report no.7: Continuing disruption of the GRS*. British Astronomical Association. Retrieved from https://britastro.org/node/18917

Sánchez-Lavega, A. (2011). *An introduction to planetary atmospheres* (pp. 273–274). Taylor-Francis, CRC Press.

Sánchez-Lavega, A., Anguiano-Arteaga, A., Iñurrigarro, P., Garcia-Melendo, E., Legarreta, J., Hueso, R., et al. (2021). Jupiter's Great Red Spot: Strong interactions with incoming anticyclones in 2019. *Journal of Geophysical Research: Planets*, *126*, e2020JE006686. https://doi.org/10.1029/2020JE006686

Sánchez-Lavega, A., Hueso, R., Eichstädt, G., Orton, G., Rogers, J., Hansen, C. J., et al. (2018). The rich dynamics of Jupiter's Great Red Spot from JunoCam – Juno images. *The Astronomical Journal*, *156*, 162. https://doi.org/10.3847/1538-3881/aada81

Sánchez-Lavega, A., Legarreta, J., García-Melendo, E., Hueso, R., Pérez-Hoyos, S., Gómez-Forrellad, J. M., et al. (2013). Colors of Jupiter's large anticyclones and the interaction of a tropical red oval with the Great Red Spot in 2008. *Journal of Geophysical Research: Planets*, *118*, 2537–2557. https://doi.org/10.1002/2013JE004371

Sánchez-Lavega, A., Orton, G. S., Hueso, R., García-Melendo, E., Pérez-Hoyos, S., Simon-Miller, A., et al. (2008). Depth of a strong Jovian jet from a planetary-scale disturbance driven by storms. *Nature*, *451*, 437–440. https://doi.org/10.1038/nature06533

Sánchez-Lavega, A., Orton, G. S., Morales, R., Lecacheux, J., Colas, F., Fisher, B., et al. (2001). The merger of two giant anticyclones in the atmosphere of Jupiter. *Icarus*, *149*, 491–495. https://doi.org/10.1006/icar.2000.6548

Sánchez-Lavega, A., Rojas, J. F., Hueso, R., Lecacheux, J., Colas, F., Acarreta, J. R., et al. (1999). Interaction of Jovian white ovals BC and DE in 1998 from Earth-based observations in the visual range. *Icarus*, *142*, 116–124. https://doi.org/10.1006/icar.1999.6197

Sculley, D. (2010). Web scale K-means clustering. In *Proceedings of the 19th international conference on World wide web*. Retrieved from https://www.eecs.tufts.edu/~dsculley/papers/fastkmeans.pdf

Shetty, S., & Marcus, P. (2010). Changes in Jupiter's Great Red Spot (1979–2006) and Oval BA (2000–2006). *Icarus*, *210*, 182–201. https://doi.org/10.1016/j.icarus.2010.06.026

Simon, A. A., Tabataba-Vakili, F., Cosentino, R., Beebe, R. F., Wong, M. H., & Orton, G. S. (2018). Historical and contemporary trends in the size, drift, and color of Jupiter's Great Red Spot. *The Astronomical Journal*, *155*, 151. https://doi.org/10.3847/1538-3881/aaae01

Simon-Miller, A. A., Banfield, D., & Gierasch, P. J. (2001). An HST study of Jovian chromophores. *Icarus*, *149*, 94–106. https://doi.org/10.1006/icar.2001.6473

Simon-Miller, A. A., Chanover, N. J., Orton, G. S., Sussman, M., Tsavaris, I. G., & Karkoschka, E. (2006). Jupiter's white Oval turns red. *Icarus*, *185*, 558–562. https://doi.org/10.1016/j.icarus.2006.08.002

Sromovsky, L. A., Baines, K. H., Fry, P. M., & Carlson, R. W. (2017). A possibly universal red chromophore for modeling color variations on Jupiter. *Icarus*, *291*, 232–244. https://doi.org/10.1016/j.icarus.2016.12.014

Taylor, F. W., Atreya, S. K., Encrenaz, T., Hunten, D. M., Irwin, P. G. J., & Owen, T. C. (2004). The composition of the atmosphere of Jupiter. In F. Bagenal, W. McKinnon, & T. Dowling (Eds.), *Jupiter: The planet, satellites and magnetosphere* (pp. 59–78). Cambridge University Press.

Toledo, D., Irwin, P. G. J., Rannou, P., Teanby, N. A., Simon, A. A., Wong, M. H., & Orton, G. S. (2019). Constraints on Uranus's haze structure, formation and transport. *Icarus*, *333*, 1–11. https://doi.org/10.1016/j.icarus.2019.05.018

Wong, M. H. (2010). *Amplitude of fringing in WFC3/UVIS narrowband red filters*. WFC3 Instrument Science Report 2010-04, STScI.

Wong, M. H., de Pater, I., Asay-Davis, X., Marcus, P. S., & Go, C. Y. (2011). Vertical structure of Jupiter's Oval BA before and after it reddened: What changed? *Icarus*, *215*, 211–225. https://doi.org/10.1016/j.icarus.2011.06.032

Wong, M. H., Marcus, P. S., Simon, A. A., de Pater, I., Tollefson, J. W., & Asay-Davis, X. (2021). Evolution of the horizontal winds in Jupiter's Great Red Spot from one Jovian year of HST/WFC3 maps. *Geophysical Research Letters*, *48*, e2021GL093982. https://doi.org/10.1029/2021GL093982

Zhang, X., West, R. A., Banfield, D., & Yung, Y. L. (2013). Stratospheric aerosols on Jupiter from Cassini observations. *Icarus*, *226*, 159–171. https://doi.org/10.1016/j.icarus.2013.05.020